Remote Sensing of Environment 248 (2020) 111972

Contents lists available at ScienceDirect

Remote Sensing of Environment

journal homepage: www.elsevier.com/locate/rse

A framework for estimating cloudy sky surface downward longwave radiation from the derived active and passive cloud property parameters

Feng Yang[a,b], Jie Cheng[a,b,*]

[a] State Key Laboratory of Remote Sensing Science, Jointly Sponsored by Beijing Normal University and Institute of Remote Sensing and Digital Earth of Chinese Academy of Sciences, Beijing 100875, China

[b] Institute of Remote Sensing Science and Engineering, Faculty of Geographical Science, Beijing Normal University, Beijing 100875, China

ARTICLE INFO

Keywords:
Surface downward longwave radiation
Cloud-base temperature
Cloud-top temperature
Cloud thickness
Single-layer cloud model
Remote sensing

ABSTRACT

The cloud-base temperature (CBT) is one of the parameters that dominates the cloudy sky surface downward longwave radiation (SDLR). However, CBT is rarely available at regional and global scales, and its application in estimating cloud sky SDLR is limited. In this study, a framework to globally estimate cloud sky SDLR during both daytime and nighttime is proposed. This framework is composed of three parts. First, a global cloudy property database was constructed by combing the extracted cloud vertical structure (CVS) parameters from the active CloudSat data and cloud properties from passive MODIS data. Second, the empirical methods for estimating cloud thickness (CT) under ISCCP cloud classification system and MODIS cloud classification system were developed. Additionally, the coefficients of CERES CT estimate models were refitted using the constructed cloud property database. With the estimated CT and reanalysis data, calculating the CBT is straightforward. The accuracy of the estimated CT for ISCCP cloud type is compared with the existing studies that were conducted at local scales. Our CT estimate accuracy is comparable to that of the existing studies. According to the validation results at ARM NSA and SGP stations, the CT estimated by the developed CT model for MODIS cloud type is better than that estimated by the original CERES CT model. Finally, the cloudy sky SDLR values were derived by feeding the estimated CBT and other parameters to the single-layer cloud model (SLCM). When validated by the ground measured SDLR collected from the SURFRAD network, the bias and RMSE are 5.42 $W{\cdot}m^{-2}$ and 30.3 $W{\cdot}m^{-2}$, respectively. This accuracy is comparable to the evaluation results of the mainstream SDLR products (Gui et al. 2010), the new evaluation results of SLCMs (Yu et al. 2018), and the accuracy of a new cloudy sky SDLR estimate method (Wang et al. 2018). All the derived CBTs improve the SDLR estimate accuracy more than the SLCM that directly uses cloud-top temperature (CTT). We will collect more ground measurements and continue to validate the developed framework in the future.

1. Introduction

The surface downward longwave radiation (SDLR) is one of the four components of the surface radiation budget (Barkstrom, 1984Cheng et al., 2018Wang and Dickinson, 2013). SDLR is a required input to land surface models, which characterize the planet's hydrological, ecological, and biogeochemical processes (Liang et al., 2010). Remote sensing is a unique means of estimating high-spatial resolution SDLR at regional and global scales. Significant progress have been achieved during the past several decades (Bisht and Bras, 2010Cheng et al., 2019Diak et al., 2000Ellingson, 1995Fu et al., 1997Gupta, 1989Kratz et al., 2020Schmetz et al., 1986Trigo et al., 2010Wang et al., 2018Wang and Liang, 2009Yu et al., 2018Zhang et al., 2004Zhou et al., 2007). To meet the requirements of the meteorological, hydrological, and agricultural research communities, i.e., a monthly averaged accuracy of 5–10 W/m^2, the acceptable accuracy of satellite-derived instantaneous SDLR is 20 W/m^2 (CEOS and WMO, 2000Gupta et al., 2004). However, the existing satellite SDLR products do not meet this accuracy requirement (Gui et al., 2010Zhang et al., 2015Zhou et al., 2011).

Much attention has been paid to the clear-sky SDLR estimate (Cheng et al., 2018Tang and Li, 2008Wang and Liang, 2009). Clouds cover approximately 67% of the Earth's surface (King et al., 2013) and overlapping cloud layers occur about 40% of the time (Wang et al., 2000). The cloudy sky SDLR consists of two parts: one part is the atmospheric longwave radiation between the cloud base and surface, and the other part is the cloud longwave radiation reaching the surface.

* Corresponding author at: State Key Laboratory of Remote Sensing Science, Jointly Sponsored by Beijing Normal University and Institute of Remote Sensing and Digital Earth of Chinese Academy of Sciences, Beijing 100875, China.
E-mail address: Jie_Cheng@bnu.edu.cn (J. Cheng).

https://doi.org/10.1016/j.rse.2020.111972
Received 23 December 2019; Received in revised form 27 June 2020; Accepted 30 June 2020

Clouds enhance SDLR by absorbing and reemitting thermal radiation emitted by the surface and beneath atmosphere (Stephens et al., 2002Takara and Ellingson, 2000). Clouds cause the greatest uncertainty in SDLR estimates (Trenberth et al., 2009Wild et al., 2001). For example, the average global cloud forcing is 31.77 W/m^2 for the period of 2003–2009 (Nussbaumer and Pinker, 2012), and this value achieves 46 W/m^2 in a previous study (Kiehl and Trenberth, 1997). The uncertainty of SDLR is considered to be remarkably larger than other components of surface radiation budget (Stephens et al., 2012Trenberth et al., 2009Wang and Dickinson, 2013). Therefore, improving the accuracy of the cloudy-sky SDLR estimate, particularly the accurate quantification of the cloud contribution, urgently needs to be solved.

A straightforward method of estimating cloudy sky SDLR is feed atmospheric information (atmospheric and water vapor profiles, cloud properties, etc.) into radiative transfer models (RTMs). RTMs have a strong physical foundation, but they require entries of many parameters and are too costly in terms of computation time (Berk et al., 1989Darnell et al., 1983Emde et al., 2016Ricchiazzi et al., 1998Wielicki et al., 1998Zhang et al., 2004Zhang et al., 1995). The remaining studies can be grouped into bulk formulae (Carmona et al., 2014Crawford and Duchon, 1999Konzelmann et al., 1994Lhomme et al., 2007Maykut and Church, 1973Trigo et al., 2010), the hybrid model (Zhou and Cess, 2001Zhou et al., 2007), the single-layer cloud model (SLCM) (Diak et al., 2000Forman and Margulis, 2009Schmetz et al., 1986Wang et al., 2018), and the multilayer cloud model (Gupta, 1989Gupta et al., 1992Gupta et al., 2010Kimball and Idso, 1982).

The bulk formula generally views the cloud and atmosphere as a whole, and the SDLR is expressed as follows:

$$SDLR = \sigma \varepsilon_{eff} T_{eff}^4 \quad (1)$$

where $\sigma = 5.67 \times 10^{-8}$ $[Wm^{-2}K^{-4}]$ is the Steffan-Boltzmann constant, ε_{eff} is effective emissivity of the atmosphere under all sky conditions, and T_{eff} is air temperature at 2 m. ε_{eff} is a function of the thermal infrared clear sky index (CSI) and air emissivity of a clear sky (Crawford and Duchon, 1999Konzelmann et al., 1994Lhomme et al., 2007). The bulk formulae only introduce CSI to correct the cloud contribution to SDLR, whereas the coefficients of the cloud correction term change continuously with total cloudiness (Niemelä et al., 2001). Therefore, this practice results in great uncertainties in the estimated cloudy sky SDLR. The hybrid method from Zhou et al. (2007) established the empirical relationship between the total precipitable water (TPW) and cloud water path (CWP, including liquid water path and ice water path) based on radiative simulation. However, CWP is not available at nighttime from the current satellite products, which limits its applications during nighttime.

Kimball and Idso (1982) and Gupta (1989) are the pioneers who developed the multilayer cloud models. The former retrieved the cloud contribution to SDLR using a four-layer cloud, which is a simple algebraic addition of the four-layer cloud longwave radiation. It is highly probable that this method will overestimate SDLR (Kimball and Idso, 1982Zhu et al., 2017). The latter is a two-layer cloud model that is adopted in the CERES radiation product (Gupta et al., 1997Kratz et al., 2020). In the calculation of SDLR, longwave radiation of the upper or lower layer is considered depending on the thickness of the top cloud (Minnis et al., 2011). Therefore, the current multilayer cloud models are actually equivalent to SLCMs in nature when calculating the cloudy sky SDLR.

CBT governs the cloud contribution to the SDLR (Gupta, 1989Schmetz et al., 1986Viúdez-Mora et al., 2015Wang et al., 2018). Theoretically, cloud base temperature (CBT) is required by the SLCM. However, current satellite cannot directly provide CBT product but cloud-top temperature (CTT). Thus, satellite derived CTT are widely used in the SLCM as a proxy (Bisht and Bras, 2011Diak et al., 2000Forman and Margulis, 2009Yu et al., 2018). This kind of SLCM is named as CTT-based SLCM. This practice will inevitably cause some additional errors in the estimated SDLR. For example, the bias and RMSE of the SDLR estimated using CTT-based SLCM (Bisht and Bras, 2011) were 12.3 W·m^{-2} and 46.1 W·m^{-2}, respectively. This accuracy cannot meet the requirements of the aforementioned applications.

The key idea of deriving CBT is to derive cloud thickness (CT, also named as cloud geometrical thickness (CGT) somewhere) or cloud-base height (CBH). Provide with the cloud-top height (CTH), CBH is calculated by minus CT from CTH. Taken satellite or reanalysis temperature profile as a reference, CBT can be calculated by linearly interpolating the referenced temperature profile with CBH (Gupta, 1989Minnis et al., 2011). There are three methods to obtain CT or CBH: (1) the LUT method (Gupta, 1989). Gupta (1989) established the look-up table (LUT) method for retrieving global CT and CBH and obtained the CBT by linearly interpolating the collocated TOVS temperature profile with CBH. This operation has great errors in terms of SDLR estimates when clouds have large vertical development, such as cumulonimbus and cirrostratus. (2) The inverse distance weighted (IDW) method (Barker et al., 2011Forsythe et al., 2000Miller et al., 2014Sun et al., 2016). The IDW method determines the contributions of surrounding active pixels to receiving pixels using the radiation similarity method or cloud type constraint and calculates the weights of these active pixels contributing to the receiving pixels based on the inverse distance method. Thus, this method is not suitable for retrieving a receiving pixel that is too far away from the active pixels (Miller et al., 2014). (3) The multiple linear regression (MLR) method (Chakrapani et al., 2002Minnis et al., 1990aMinnis et al., 2011Minns et al., 1992). Minnis et al. (2011) built the relationship between CT and cloud optical thickness (COT) and cloud center temperature (CCT) for the MODIS-derived liquid water cloud and ice water cloud, and then, CBT is derived by interpolating the ECWMF temperature profile with CBH. The cloud types (i.e., MODIS-derived mixed phase cloud and undetermined phase cloud or ISCCP-derived altocumulus, altostratus, nimbostratus, cirrostratus, and cumulonimbus) are not completely considered in the present research (Chakrapani et al., 2002Minnis et al., 2011), and thus, the global coverage is not complete; meanwhile, the MLR method was developed at small scale (Chakrapani et al., 2002Minnis et al., 1990aMinns et al., 1992), which may not be applicable at the global scale; Apart from their respective drawbacks, the current CT models cannot well estimate CT during nighttime. In addition, the Visible infrared Imaging Radiometer (VIIRS) provides the CBH product, which is defined as the height above mean sea level of the base of the uppermost cloud layer (Miller et al., 2019). Thus, VIIRS CBH cannot be used in the calculation of SDLR under multilayer cloudy condition. This forces us to seek a new CT estimation method to accurately obtain global CT or CBH during both daytime and nighttime.

The main purpose of this study is to develop a framework for estimating the cloudy sky SDLR, which includes (1) proposal of a global CT estimation method that can be used in both daytime and nighttime; and (2) improvement of the SLCM performance via correcting the overestimation phenomenon dealing with the low-level cloud. The structure of this manuscript is organized as follows: the datasets used are described in Section 2; the methods for constructing the cloud property database, estimating CT and CBT, and the cloudy-sky SDLR are introduced in Section 3; the results are presented in Section 4; Section 5 provides the merits and shortcomings of the developed CT estimation method. The estimated SDLR is compared with that derived from the three categories of CBT-based SLCMs in this section; and finally, the conclusion is provided in Section 6.

2. Datasets

The data used primarily consist of three parts: (1) Satellite data for extracting the cloud vertical structure (CVS) parameters, cloud property parameters, and latitude; (2) Satellite and reanalysis data. for generating the inputs to the SLCM, and (3) Ground measured CVS parameters and SDLRs. Table 1 summarizes the characteristics of the

Table 1
Satellite data and reanalysis data used in this study.

Data sources	Product name	Spatial Resolution	Parameters	Function
MODIS	MYD03	1 km	Latitude, Longitude	Calculate CTs, CBHs, and cloudy sky SDLRs
	MYD06_L2	5 km	Cloud fraction (CF) Cloud top pressure (CTP) Cloud top height (CTH) Cloud effective emissivity (CEE) Cloud top temperature (CTT) Cloud phase infrared (CPI)	
		1 km	Cloud optical thickness (COT) Cloud effective radius (CER)	
	MYD35_L2	1 km	Cloud mask (CM)	
	GMTED	7.5 “	Elevation	Map spatial distribution of surface elevation
CloudSat	2B-CLDCLASS-LIDAR.P1_R05	1.4 × 1.8 km	TAI_Time, Latitude, Longitude CloudLayerTop (CLT) CloudLayerBase (CLB)	Train and test CT models
	MOD06-1KM-AUX.P1_R05	1 × 1.8 km	Cloud_Phase_Infrared_1km Cloud_top_pressure_1km Cloud_top_temperature_1km Cloud_emissivity_1km Cloud_Effective_Radius Cloud_Optical_Thickness	
Merra-2	inst6_3d_ana_Np	0.5° × 0.625°	Vertical level, latitude, Longitude Specific humidity, air temperature	Calculate CBTs and cloudy sky SDLRs
	statD_2d_slv_Nx	0.5° × 0.625°	Surface_pressure, Latitude, Longitude 2-m air temperature Dew point temperature at 2 m	

satellite data and reanalysis data.

2.1. Satellite data

Four years (2012–2015) of Aqua-MODIS products, i.e., MYD03, MYD06, and MYD35 were downloaded from the NASA Land Process Distributed Active Archive Center (http://lpdaac.usgs.gov/). MYD03 provides geolocation data (latitude and longitude) at a 1 km spatial resolution, and these data were used to match different datasets. MYD06 provides various cloud property parameters, such as COT, CER, CTT, and CEE (King et al., 1997Menzel et al., 2015). These parameters were used to train and test the developed CT model, as well as estimate cloudy sky SDLR. MYD35_L2 are used to identify cloud sky pixels (Ackerman et al., 2010).

The 2010 Global Multiresolution Terrain Elevation Data was downloaded from the United States Geological Survey (http://topttols.cr.usgs.gov/gmted_viewer/). GMTED2010 was produced by combing multiple high-quality DEM datasets from various international institutions with a spatial resolution of 7.5 arc-seconds (Danielson and Gesch, 2011). GMTED2010 was used to map the spatial distribution of global land surface elevations.

The CloudSat, CALIPSO and Aqua satellites all belong to the A-train constellation. The former two lag behind the latter by 1 to 2 min (Seemann et al., 2008). CloudSat and CALIPSO are separated from each other by 10 to 15 s, leading to a synergistic instrument suite view of the same cloud area at nearly the same moment. CALIPSO lidar and CloudSat radar are complementary with each other and have different advantages to measure different types of clouds from space (Wang and Sassen, 2007). CALIPSO lidar is more sensitive to detecting optically thin upper tropospheric clouds, while CloudSat radar provide a better coverage for optically thick clouds. 2B-CLDCLASS-LIDAR.P1_R05 combines CloudSat CPR and CALIPSO lidar measurements to classify clouds into the largest 10 layers for each cloudy pixel (Stephens et al., 2008Wang, 2019). As shown in Table 1, five parameters (i.e., TAI_Time, Latitude, Longitude, CLT, and CLB) from 2B-CLDCLASS-LIDAR.P1_R05 are used in this study. TAI_Time, Latitude, and Longitude were used to match other datasets, and CLT and CLB were used to retrieve the active CT. Note that 2B-CLDCLASS-LIDAR.P1_R05 was downloaded from ftp1.cloudsat.cira.colostate.edu. The CloudSat auxiliary data product (MOD06-1KM-AUX.P1_R05) has matched CloudSat bins with MYD06, and thus, this study directly used this product instead of MYD06 when training and testing the CT model.

2.2. Reanalysis data

Merra-2 provides data beginning in 1980 with a spatial resolution of 0.5° × 0.625°, and it assimilates the meteorological data from a modern satellite database. Merra-2 includes an interactive analysis of aerosols that feed back into the circulation, it uses NASA's observations of stratospheric ozone and temperature (when available), and it takes steps towards representing cryogenic processes (Gelaro et al., 2017). Merra-2, which includes temperature and specific humidity (QV) profiles at 42 levels from 1000 to 0.1 hPa, was used to derive CBT at the CBH location. The air emissivity was calculated from 2-m air temperature and dew point temperature. TPW was calculated from Merra-2 and used to analyze its contribution to SDLR.

2.3. Site observations

There are two types of site observed data: one is the Atmospheric Radiation Measurement (ARM) Mace PI Product (Mace et al., 2009Mao et al., 2018), the other is the ground measured SDLR from SURFRAD network (Augustine et al., 2000).

The ARM Mace PI product are produced from lidar, ceilometer, and cloud radar measurements. The North Slope of Alaska Barrow site (NSA, 71.3177°N, 156.605°W) and the Southern Great Plains Lamont site (SGP, 36.605°N, 97.485°W) were used to obtain the ground measured CT and validate the developed CT estimate models in Section 3.2. The corresponding climate features of the sites are gradually cold and dry climate and mild climate, respectively. In addition, time of the used Mace PI products are 2010 and 2009, respectively.

As shown in Fig. 1, the ground measured SDLR collected from the SURFRAD network (Augustine et al., 2000) was used to evaluate the estimated cloudy sky SDLR. The SURFRAD sites can provide continuous and long-term ground-based radiation measurements beginning in 1995 for the earliest established site, and the corresponding data can be downloaded at http://www.srrb.noaa.gov/surfrad/. The radiation data are archived as daily files with a 3-min and 1-min average before and

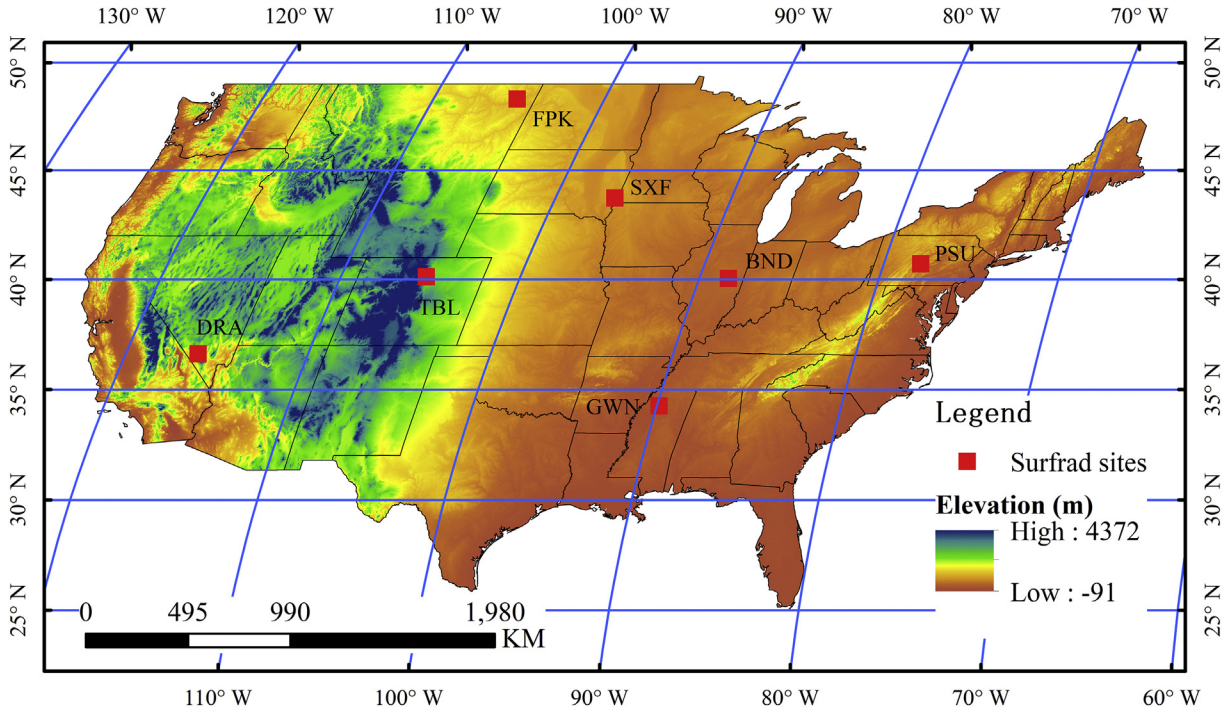

Fig. 1. Spatial distribution of the sites in the SURFRAD network.

Table 2
Descriptions of site conditions in the SURFRAD network.

Code	Site name	Lat & Lon (degree)	Elevation (m)	Land cover	Temporal resolution	Temporal period
BND	Bondville	40.05, −88.37	230	Grassland	1 min	2013 to 2015
DRA	Desert Rock	36.63, −116.02	1007	Arid shrub land	1 min	2013 to 2015
FPK	Fort Peck	48.31, −105.10	634	Grassland	1 min	2013 to 2015
GWN	Goodwin Creek	34.2547, 89.87	98	Grassland	1 min	2013 to 2015
PSU	Penn. State	43.73, −96.62	376	Cropland	1 min	2013 to 2015
SXF	Sioux Falls	43.73, −96.62	473	Grassland	1 min	2013 to 2015
TBL	Table Mountain	40.13, −105.24	1689	Sparse grassland	1 min	2013 to 2015

after January 1, 2009, respectively. The SDLR measurements of SURFRAD cover a spectral range of ~4.0 to 50 μm and with an accuracy of ± 9 $W{\cdot}m^{-2}$ (Augustine et al., 2000). The time range of SURFRAD SDLR observations used in this study is from 2013 to 2015. Detailed site information is provided in Table 2.

3. Methodology

There are three parts in this section. First, a cloud property database was constructed by combining extracted CVS and cloud property parameters. Then, we established an empirical model for CT estimations and calculated CBH and CBT using estimated CT and reanalysis data in the following section. Finally, cloudy sky SDLR was estimated using the single-layer cloud model and sensitivity analysis was performed from SimLab. Fig. 2 shows the flowchart for retrieving CT and cloudy sky SDLR.

3.1. Constructing the cloud property database

According to the study by Minnis et al. (2011), CTT can better represent the cloud top properties, and COT and CER are the representative variables for cloud optical and microphysical properties. Due to MODIS cloud optical and microphysical properties being unavailable at nighttime, this study chose the CTT, COT, and CER cloud properties in daytime, and CTT and CEE are used as the cloud properties at nighttime. 2B-CLDCLASS-LIDAR.P1_R05 provides CLB and CLT of each layer for a multiple-layer cloud system. The cloud property database was constructed with the following steps:

(1) Spatial and temporal matching. Even 2B-CLDCLASS-LIDAR.P1_R05 and MOD06-1KM-AUX.P1_R05 are collocated with each other, we conducted the spatial and temporal matching to ensure the accuracy of the collocation. Then, the cloud-base height, cloud-top height and cloud type of each layer, the number of cloud layers, overpass time, latitude, longitude, elevation, and flag of land and sea of each pixel were extracted from 2B-CLDCLASS-LIDAR.P1_R05; COT, CER, CTT, CTP, CEE, CF, and CPI of that pixel are extracted from MOD06-1KM-AUX.P1_R05.
(2) Cloud pixels identification. If the cloud fraction is larger than zero, the pixel was labeled as cloud pixel.
(3) CT calculation. The CT of each cloud layer was calculated by subtracting CLB from CLT and the entire CT of the cloud was the sum of the CTs of the multiple-layer clouds.
(4) Day and night classification. With the sunrise and sunset time calculated from the latitude, longitude and Julian day of the satellite overpass time, we can label the cloudy pixel as daytime pixel or nighttime pixel.

Finally, through the above operations, we completed the construction of the cloud product database using four years of CloudSat products. There are 243,945,283 samples in the constructed database. Each sample contains CVS parameters (CLB and CLT), cloud property

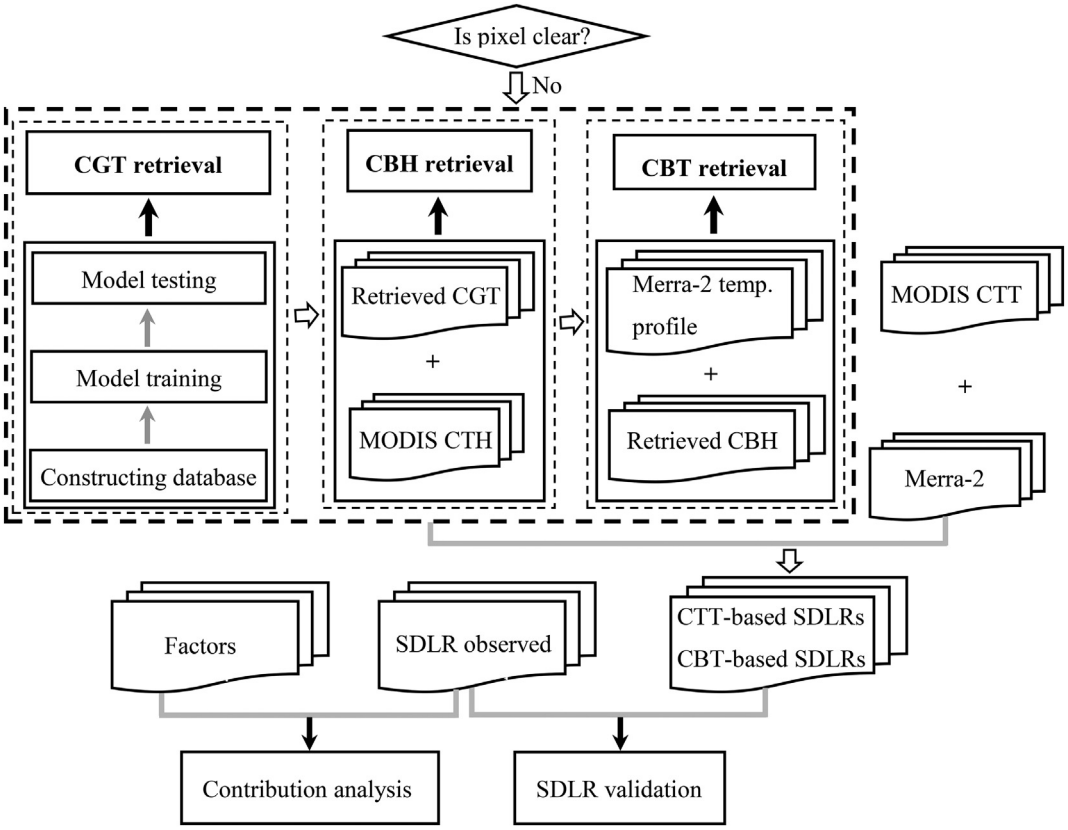

Fig. 2. The flowchart for retrieving CT and cloudy sky SDLR.

Table 3
ISCCP and MODIS cloud classification systems.

Cloud classification system	Cloud types	
ISCCP	Low-level	Stratus, stratocumulus, cumulus
	Mid-level	Nimbostratus, altostratus, altocumulus
	High-level	Cirrus, cirrostratus, cirrocumulus
MODIS	Water cloud, ice cloud, mixed phase cloud, and undermined phase	

parameters (CTT, CTP, CEE, CPI, COT, and CER), and CT calculated from the CVS data.

3.2. Estimates of CT and CBT

3.2.1. Rationality of the CT estimate

The same types of clouds (e.g., ISCCP-derived cirrus, cumulus, and stratocumulus, or MODIS-derived ice and liquid water clouds) often share geometric, microphysical, and radiative and thermodynamic properties at the regional scale, and these characteristics obey a certain spatial distribution rule (Barker et al., 2011Forsythe et al., 2000Miller et al., 2014Stowe et al., 1999). The reason may be that the atmospheric conditions of forming a particular type of cloud may represent conditions that exist well beyond the spatial range of an individual cloud element for a given region. This phenomenon generally ties to airmass properties (Holton, 1973), which vary on a much broader spatial scale. Additionally, numerous studies have demonstrated that the CT has a close relationship with cloud microphysical properties (COT, CER, and CWR), and radiative and thermodynamic properties (CTT and CEE) for the same cloud type (Chakrapani et al., 2002Minnis et al., 1995Minnis et al., 1990b). As a result, we can relate cloud geometric characteristics (such as CBH, CTH, and CT) to other cloud properties, such as COT, CER, CTT, and CEE, at the regional scale.

However, water vapor and temperature exhibit significant spatial variabilities but have a certain spatial distribution rule at global-scale, particularly in the latitudinal direction, which is related to airmass properties. In other words, there are some different air mass distribution patterns from the poles to the equator (Willett, 1933), which is closely related to the latitude value. Thus, we need to add latitude as a predictor when establishing the relationship between CT and cloud properties at the global scale to mitigate large regional jumps.

3.2.2. CT estimates

Currently, there are two different cloud classification systems (Table 3): The International Satellite Cloud Climatology Project (ISCCP) cloud classification system and the MODIS cloud classification system (abbreviated later as the ISCCP cloud type and MODIS cloud type). We adopted the ISCCP cloud type and MODIS cloud type as the statistical constraints and developed the ISCCP cloud type and MODIS cloud type CT estimation models, respectively. Note that we divided the MODIS cloud types into four types (Menzel et al., 2015Minnis et al., 2011), i.e., water-clouds1 (CPI = 1 and COT > 1), water-clouds2 (CPI = 1 and COT ≤1), ice clouds and other clouds (mixed phase cloud and undermined phase) in this study. The general formulae are expressed as follows:

$$CT_{ISCCP-day1} = a_0 + a_1 lnCOT + a_2 CER + a_3 CTT + a_4 \mathrm{abs}(lat)\ (if\ COT > 3.6) \quad (2)$$

$$CT_{ISCCP-day2} = b_0 + b_1\sqrt{COT} + b_2 CER + b_3 CTT + b_4 \mathrm{abs}(lat)\ (if\ COT \le 3.6) \quad (3)$$

$$CT_{MODIS-day1} = c_0 + c_1 lnCOT + c_2 CER + c_3 CTT + c_4 \mathrm{abs}(lat)\ (if\ COT > 1) \quad (4)$$

$$CT_{MODIS-day2} = d_0 + d_1\sqrt{COT} + d_2 CER + d_3 CTT + d_4 \mathrm{abs}(lat)\ (if\ COT \le 1) \quad (5)$$

$$CT_{MODIS-night} = e_0 + e_1 CTT + e_2 \mathrm{abs}(lat) + e_3 CEE \quad (6)$$

where Eqs. (2) and (3) are the CT estimation models for the ISCCP cloud type; Eqs. (4) and (5) are the CT estimation models for the MODIS cloud type during daytime, while Eq. (6) is the CT estimation model for the MODIS cloud type during nighttime; a_0, a_1, a_2, a_3, a_4, b_0, b_1, b_2, b_3, b_4, c_0, c_1, c_2, c_3, c_4, d_0, d_1, d_2, d_3, d_4, e_0, e_1, e_2, and e_3 are regression coefficients. Note that the thresholds of COT in Eqs. (2)–(5) are referred to Doutriaux-Boucher and Sèze (1998) and Minnis et al. (2011).

The original coefficients of the CERES CT models during daytime are fitted in small regions using the MODIS cloud type classification system (Minnis et al., 2011) and may not be applicable at the global scale, so we refitted the coefficients of the CERES CT estimation model using the constructed cloud property database in this study. The general formulations of the CERES CT models (Minnis et al., 2011) are expressed as follows:

$$CT = a_1 lnCOT + a_2\ (if\ CPI = 1\ and\ COT > 1) \quad (7)$$

$$CT = b_1 COT^{b_2}\ (if\ CPI = 1\ and\ COT \le 1) \quad (8)$$

$$CT = c_1 - c_2 CTT + c_3 lnCOT\ (if\ CPI = 2\ and\ CTT \le 245) \quad (9)$$

where a_1, a_2, b_1, b_2, c_1, c_2, and c_3 are regression coefficients. Also, we compared the performance of CERES CT models using the refitting coefficients and original coefficients. The comparison results are shown in Section 4.2.1 of the revised manuscript.

3.2.3. CBT estimates

To obtain CBT, we first estimate CBH, and then linearly interpolate the collocated reanalysis temperature profile in time and pressure. CBH can be calculated by subtracting the estimated CT from the MODIS CTH, i.e., CBH = CTH − CT. However, there may exist a few unreasonable CBHs because of the singular values of inputs to the CT model. Therefore, several criteria are used to process the estimated CTs and CBHs (Minnis et al., 1995). If CT < 0.1, then CT is reset to 0.1 km. If CBH is less than the ground elevation, then CBH is reset to CBH = CBH + 0.1 km. These steps are repeated if necessary. Note that the unit of estimated CBH is km, which is converted to pressure units using the formula provided at http://www.engineeringtoolbox.com/air-altitude-pressure-d_462.html. Reanalysis temperature profiles for two different forecast times were interpolated to the satellite time using linear interpolation with time differences. Next, CBT was derived from the aforementioned interpolated reanalysis temperature profile with CBH. Note that the estimated CBT is difficult to validate directly, so the estimated CBT are not shown in section 4, and the histograms of estimated CBT are displayed in section 5.2.

3.3. Single-layer cloud model and sensitivity analysis

3.3.1. Single-layer cloud model

The general form of SDLR under the framework of SLCM is expressed as (Diak et al., 2000Kimball and Idso, 1982Schmetz et al., 1986Wang et al., 2018):

$$SDLR = \sigma\varepsilon_a T_a^4 + \sigma\varepsilon_c T_c^4 \times (1 - \varepsilon_a) \times cf \quad (10)$$

where $\sigma = 5.67 \times 10^{-8}$ $[Wm^{-2}K^{-4}]$ is the Steffan-Boltzmann constant, ε_a is clear sky air emissivity, T_a is air temperature at screen level, ε_c is cloud effective emissivity and is set to 1, T_c is cloud base temperature, and cf is cloud fraction. The first item on the right of Eq. (10) represents the contribution of the atmosphere between the cloud base and surface, and the second item describes the cloud contribution to SDLR. Note that ε_a is usually calculated by the bulk scheme of Prata (1996) because of its high accuracy in estimating clear sky SDLR (Bisht and Bras, 2010Diak et al., 2000Guo et al., 2019Wang and Dickinson, 2013Yu et al., 2018), which is expressed as follows:

$$\varepsilon_a = 1 - (1 + \xi)\, exp(-\sqrt{1.2 + 3\xi}) \quad (11)$$

$$\xi = \frac{46.5}{T_a} e_0 \quad (12)$$

$$e_0 = 6.11 \exp\left[\frac{L_v}{R_v}\left(\frac{1}{273.15} - \frac{1}{T_d}\right)\right] \quad (13)$$

where $L_v = 2.5 \times 10^6$ $[kg^{-1}]$ is the latent heat of vaporization, and $R_v = 461$ $[kg^{-1}K^{-1}]$ is the gas constant for water vapor.

SDLR is overestimated for the low-level cloud cover (Bréon et al., 1991Gupta et al., 1992Schmetz et al., 1986). For example, Bréon et al. (1991) and Gupta et al. (1992) found that the method of Gupta (1989) overestimated SDLR when $P_s - P_{cb} \le 200$ hPa (low-level cloud scenario), where P_s is the surface pressure and P_{cb} is cloud-base pressure (CBP). Actually, the method of Gupta (1989) is an SLCM (Minnis et al., 2011). Therefore, this study corrects the overestimation phenomenon of SLCM estimated SDLR for low-level cloud cover conditions. Inspired by the study of Gupta et al. (1992), we calculate the maximum and minimum cloud contributions to SDLR for low-level cloud cover condition in Eq. (10), denoted as *SDLR_cloud_max* and *SDLR_cloud_min*, respectively. The final low-level cloudy sky SDLR is linearly interpolated between *SDLR_cloud_max* and *SDLR_cloud_min* using CBP. When cloud base is located near the surface, *SDLR_cloud_max* can be expressed as follows:

$$SDLR\_cloud\_max = (\sigma T_a^4 - \sigma\varepsilon_a T_a^4) \times (1 - \varepsilon_a) \times \mathrm{cf} \quad (14)$$

Additionally, when CBP = P_{upper}, which is a low-level cloud upper boundary, SDLR_cloud_min is calculated by the following equation:

$$\mathrm{SDLR\_cloud\_min} = \sigma\varepsilon_c T_c^4 \times (1 - \varepsilon_a) \times cf \quad (15)$$

(Several criteria are required to determine the low-level cloud upper boundary (Doutriaux-Boucher and Sèze, 1998). If $P_s > 680$ hPa, the upper boundary of the low cloud is reset to 680 hPa; otherwise the upper boundary of the low-level cloud is reset to 440 hPa.

3.3.2. Sensitivity analysis

To better understand the effect of the cloud property parameters (COT, CER, and CBH) on the estimated cloudy sky SDLR, a global sensitivity analysis (GSA) was performed by using the software SimLab (http://simlab.jrc.ec.europa.eu). Seven parameters listed in Table 4 were input to SimLab and generated 1967 combinations assuming a uniform distribution between the lower and upper bounds for each parameter. These combinations were input to the Santa Barbara DISORT Atmospheric Radiative (SBDART) model to simulate the cloud sky SDLR(Ricchiazzi et al., 1998). The built-in US62 standard atmospheric vertical profile and the default values of other parameters provided in SBDART User guide (2007) SBDART, 2007 were adopted in the simulation. The matchup of input parameters and simulated SDLR were then input to SimLab, and the built-in Extended Fourier amplitude sensitivity test (EFAST) model was chosen for sampling and sensitivity analysis (Saltelli et al., 1999). The total sensitivity index, which expresses the total contribution of this factor to the output variance when

Table 4
Parameters used for generating the inputs of SBDART.

Parameter	Implication	Units	Range
TPW	integrated water vapor amount	g/cm^2	0.8–3.0
UO_3	integrated ozone concentration	atm-cm	0.1–0.6
CO_2	volume mixing ratio of CO_2	ppmv	360–390
COT	Optical thickness of cloud layer	–	0–128
CBH	Altitude of cloud layer base	km	0–9
CER	Cloud drop effective radius	micron	2–60
VIS	Horizontal path visibility	km	2–100

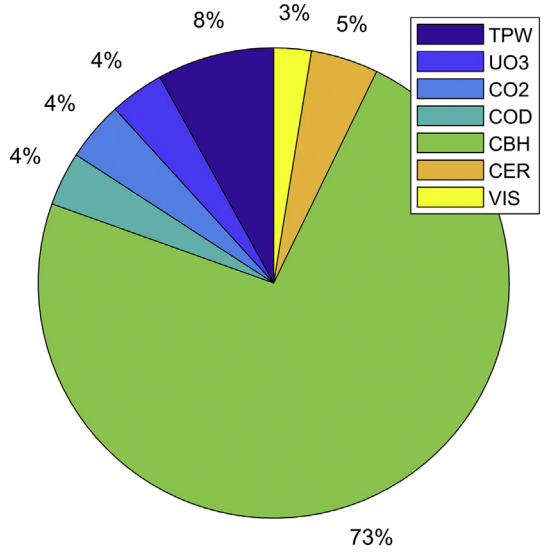

Fig. 3. Normalized total sensitivity index of each parameter in Table 4.

the other factors' interactions have also been calculated, was used to determine each factor's sensitivity. Fig. 3 shows the sensitivity analysis results. CBH has the largest total sensitivity index of 73%, whereas the total sensitivity indexes of other parameters are around 5%, which indicates that CBH plays the most import role in the estimated cloudy sky SDLR.

4. Results

4.1. Spatial-temporal distributions of samples in the cloud property database

In total, we obtained 243,945,283 samples using four years of satellite data, including 135,820,004 samples in daytime and 108,125,279 samples at nighttime. We randomly divided the samples into two parts: two-thirds of these samples were used to train the CT estimate models, while the remaining one-third of samples were used to test the developed models. Table 5 shows the spatial-temporal distributions of the training samples that are used to develop the CT estimate models. The number of samples for most of the seasons in the latitudinal zones are larger than 37,804 except for DJF in the 75–90°N zone during daytime and JJA in the 75–90°S zone during both daytime and nighttime, which indicated that the temporal distribution of samples is uniform in most cases.

Fig. 4 shows the spatial distribution of training samples for each cloud type in the ISCCP cloud type during daytime. It is found that the cumulus and stratocumulus samples are mainly located in the marine area; the stratus and nimbostratus samples mainly distribute in the high altitudes; the altocumulus and altostratus samples are mostly scattered near 0°, 50° N, and 50° S; the cirrus, cirrostratus, and cumulonimbus samples are largely distributed between 50° N and 50° S. Note that a two cloud classification system is used in this study, and the spatial-temporal distributions of the training samples may be different. Here, we only show the spatial distribution of the training samples for the ISCCP cloud type during daytime for simplicity. The spatial-temporal distributions of the samples for testing the developed CT estimate models are similar to those used for developing the CT estimate models.

4.2. Performance of CT estimate models

4.2.1. Cloud type based CT estimate models

Using two-thirds of the samples selected randomly from the constructed cloud property database, we fit Eqs. (2)–(9) and obtained their coefficients. Each formula and the coefficient for each variable were significant below the confidence level of $P < .001$ with the exception of water-clouds2. The fitting results are show in Tables 6-8. Overall, considering the coefficients of the CT estimate models, CER and COT are positively correlated with the CT estimate, while latitude, CTT, and CEE are negatively correlated with the CT estimate. Table 6 lists the training results of the MODIS cloud type CT estimate models. During daytime, the water clouds (water-clouds1 and water-clouds2) CT model has the best performance with the lowest RMSEs of 0.87 and 0.83 km, respectively, while the ice clouds CT model has the worst performance with the largest RMSE of 2.09 km. The performance of other clouds CT model is intermediate between the water clouds CT model and the ice clouds CT model with an RMSE of 1.68 km. This may be caused by the cloud multilayer effects, i.e., some ice clouds identified by CPI often contain water clouds beneath them and the clouds in the column are assumed to be composed entirely of ice. During nighttime, the CT models perform slightly worse than the corresponding CT models during daytime, which may be caused by the fewer CT model inputs (only CTT and CEE) used to predict CT.

Table 7 provides the accuracy of ISCCP cloud type CT models. CT models for ISCCP low-level clouds have the best performance with RMSEs of 0.96–1.14 km, followed by CT models for ISCCP mid-level clouds and ISCCP high-level cirrus clouds with RMSEs of 1.45–1.58 km, and finally, CT models for ISCCP high-level cirrostratus and cumulonimbus clouds have RMSEs of 2.07–2.10 km. Note that the ISCCP high-level cirrus CT model performs similarly to the ISCCP mid-level CT models. This can be partially explained by the fact that that the low-level clouds are more likely to be water clouds, and the high-level clouds are more likely to be ice clouds. Regarding R^2 of ISCCP low-level clouds and high-level clouds, the smaller the COT value is, the larger the R^2, and vice versa for ISCCP high-level clouds. The biases of all ISCCP cloud type CT models are less than 0.0068 km.

Table 8 lists the fitting results for the CERES CT models. The CT models for water-clouds1 and water-clouds2 perform better than that for ice clouds, with RMSEs of 1.10, 1.10, and 2.50 km, biases of −7.2E-15, −0.088, and − 0.16 km, successively. Note the same cloud types

Table 5
The distribution of the training samples for different seasons and latitudinal zones. (DJF is the abbreviation for December, January, and February; MAM is the abbreviation for March, April, and May; JJA is the abbreviation for June, July, and August; and SON is the abbreviation for September, October, and November).

Latitude/season	Daytime				Percent	Nighttime				Percent
	DJF	MAM	JJA	SON		DJF	MAM	JJA	SON	
75–90°N	0	1,657,895	4,412,476	17,609,213	16.77%	2,934,831	2,365,077	2,097,632	15,491,866	21.78%
45–75°N	2,672,364	3,963,327	6,640,393	19,005,016	14.62%	3,524,871	5,772,204	8,671,008	15,971,894	13.63%
15–45°N	3,345,831	2,907,469	3,813,881	18,067,331	15.24%	1,565,090	1,818,935	3,225,324	14,627,428	14.11%
15S°-15°N	3,463,188	3,071,685	4,464,114	18,319,662	15.60%	2,339,520	2,247,741	2,666,036	14,742,643	12.73%
15–45°S	3,731,131	3,419,787	4,524,286	18,351,976	16.02%	1,673,699	1,574,257	2,073,152	14,514,572	12.56%
45–75°S	5,839,699	3,503,658	2,750,425	18,739,865	9.44%	1,688,707	1,402,072	1,741,322	14,747,964	10.51%
75–90°S	1,140,700	37,804	0	16,984,789	12.31%	1,977,962	263,973	0	14,139,130	14.69%
Percent	10.49%	9.65%	13.83%	66.04%	55.25%	10.08%	9.91%	13.14%	66.88%	44.75%

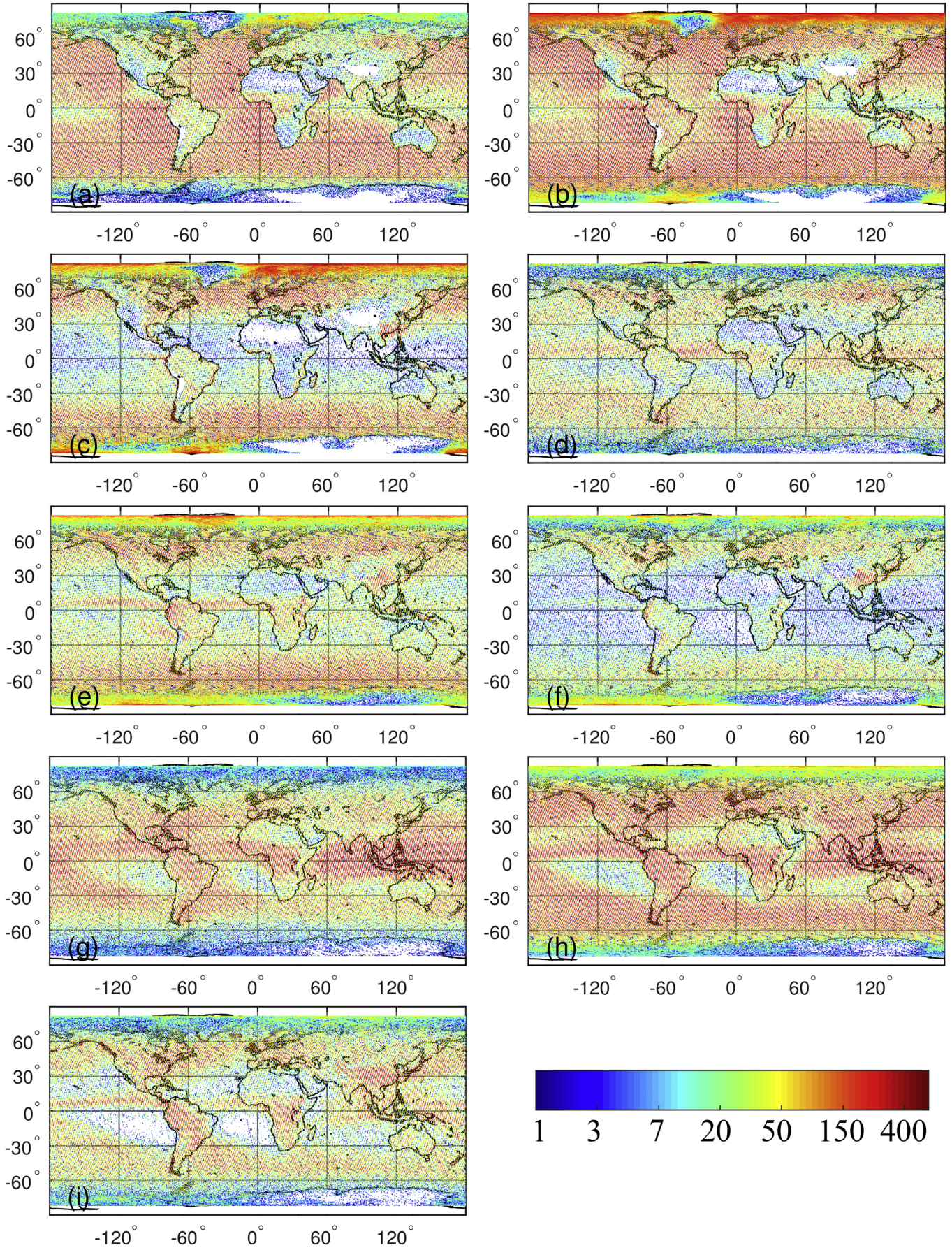

Fig. 4. Spatial distribution of samples in the constructed database that are used to develop the ISCCP cloud type CT estimate models during daytime. The subplots (a)-(i) are cumulus, stratocumulus, stratus, altocumulus, altostratus, nimbostratus, cirrus, cirrostratus and cumulonimbus, respectively.

Table 6
The fitting results of the CT estimation models using MODIS cloud types.

Time	Cloud type	Count	Const	coef_cod	coef_cer	coef_ctt	coef_lat	coef_cee	RMSE (km)	bias (km)	R^2
Daytime	Water-clouds1	33,515,045	11.2704	0.2239	0.0600	−0.0393	−0.0169	NA	0.87	0.014	0.29
	Water-clouds2	338,581	5.4206	0.3547	0.0360	−0.0190	−0.0005	NA	0.83	0.0006	0.39
	Ice-clouds	44,880,526	14.2773	1.3414	0.1019	−0.0594	−0.0136	NA	2.09	0.038	0.57
	Other-clouds	11,312,279	13.8756	0.6254	0.0820	−0.0480	−0.0398	NA	1.68	0.018	0.49
Nighttime	Water-clouds	16,670,799	14.2078	−0.4061	NA	−0.0432	−0.0171	−0.4061	0.93	0.0009	0.11
	Ice-clouds	16,206,415	24.4160	3.2212	NA	−0.0927	−0.0054	3.2212	2.21	0.0019	0.26
	Other-clouds	7,750,730	15.8096	−2.5316	NA	−0.0302	−0.0509	−2.5316	1.75	0	0.18

Table 7
The fitting results of the CT estimation models using ISCCP cloud types.

Cloud level	Cloud type	Count	Const	coef_cod	coef_cer	coef_ctt	coef_lat	RMSE (km)	bias (km)	R^2
Low cloud	Cumulus	8,031,299	11.5435	0.0404	0.0517	−0.0401	−0.0040	0.96	0.0068	0.43
	Stratocumulus	26,891,360	9.5965	0.0686	0.0655	−0.0340	−0.0057	0.99	0.0016	0.23
	Stratus	5,800,174	3.7159	0.4178	0.0544	−0.0162	−0.0019	1.14	0	0.12
Middle cloud	Altocumulus	2,225,242	9.4921	0.8738	0.0441	−0.0381	0.0183	1.52	0.0003	0.39
	Altostratus	8,804,747	14.7270	0.4213	0.0875	−0.0544	−0.0081	1.50	0	0.43
	Nimbostratus	4,127,788	13.2535	0.2997	0.0703	−0.0448	−0.0150	1.58	0	0.20
High cloud	Cirrus	9,685,130	7.1732	2.0011	0.0421	−0.0352	0.0176	1.45	0	0.25
	Cirrostratus	18,165,456	15.9730	1.9982	0.1169	−0.0745	−0.0100	2.07	0.0010	0.50
	Deep-convection	5,723,675	33.4008	0.4785	0.1160	−0.1221	−0.0500	2.10	0	0.69

Table 8
The refitting results of the CERES CT estimation models using MODIS cloud types.

Cloud type	Count	Const	coef_ctt	coef_cod	RMSE (km)	bias (km)	R^2
water-clouds1	33,515,045	0.4401	NA	0.2937	1.10	−7.2E-15	0.07
water-clouds2	338,581	NA	NA	1.4217	1.10	−0.0880	−0.15
ice-clouds	31,282,706	23.3319	−0.0869	1.0610	2.50	−0.1600	0.39

are adopted in MODIS CT models and CERES CT models. However, CERES CT models cannot include CT models during nighttime. This may be because CERES CT models depend greatly on COT as a CT model input.

Overall, the comparison of the training results of MODIS and ISCCP cloud type CT estimate models shows that the developed CT models for ISCCP low-level cloud types have comparable accuracy with those for MODIS water clouds, while performances of the CT models for ISCCP high-level cirrostratus and cumulonimbus clouds are similar to those for MODIS ice clouds; the CT models of ISCCP mid-level clouds have slightly better accuracy than that of other MODIS clouds. Additionally, although CERES CT models have the same cloud types (i.e., water-clouds1, water-clouds2, and ice clouds) as the MODIS cloud type CT models, the CERES CT models perform relatively worse than the corresponding CT models of MODIS cloud types.

The developed CT estimation models were tested using the remaining one-third of samples. Figs. 5-7 display the testing results. Overall, most of the fitting lines for the CT estimates using MODIS cloud types and ISCCP cloud types deviate from the 1:1 line, and the dynamic range of predicted CT is smaller than the observed CT except for ISCCP high-level cumulonimbus. Fig. 5 shows the testing density scatter plots for CT estimates using MODIS cloud type. During daytime, the density scatterplots for water-clouds1 and water-clouds2 had the best concentrated distribution with a range of 0–3 km, followed by that of other-clouds and ice-clouds with ranges of 0–4 km and 0–10 km, respectively. During nighttime, the density scatterplots for water-clouds, other-clouds, and ice-clouds had similar distributions to that during daytime. This indicates that ice clouds have larger CT variation range than water clouds. Table 9 summarizes the accuracy of the CT estimates using MODIS cloud type. During daytime, all MODIS cloud type CT models had slight overestimation phenomena with biases of less than 0.038 km. During nighttime, the water-clouds CT model had slightly overestimated CT results with a bias of 0.0011 km, while the CT models for ice-clouds and other-clouds had slightly underestimated CT results with biases from $-8.9e^{-5}$ to $-2.8e^{-5}$ km. Although CTs were slightly overestimated or underestimated, the biases were very low. This indicated that MODIS CT estimate models perform well as a whole. The RMSE values of the CT models for water-clouds, ice-clouds, and other-clouds were 0.85 and 0.96 km, 2.1 and 2.2 km, and 1.7 and 1.8 km, respectively. The results are consistent with that from the training phase.

Fig. 6 shows the testing density scatter plots for CT estimates using the ISCCP cloud type. The density scatter plots for the ISCCP low-level clouds, ISCCP mid-level clouds and ISCCP high-level cirrus clouds, and ISCCP high-level cirrostratus and cumulonimbus clouds had in turn the concentrated distribution ranging from 0 to 3 km, 0 to 6 km, and 0 to 12 km, respectively. This presents a certain correspondence with MODIS water clouds and ice clouds. Table 10 lists the accuracies of the ISCCP cloud type CT models. Overall, the bias for each cloud type was very small. Specifically, the CT models for stratus, nimbostratus, and cirrus clouds had slightly underestimated CTs with biases of −0.00081 – −0.00015 km, while the other CT models had slightly overestimated CTs with biases of 0.00061–0.0065 km. The RMSEs of the CT models for ISCCP low-level clouds, ISCCP mid-level clouds and ISCCP high-level cirrus clouds, and ISCCP high-level cirrostratus and cumulonimbus clouds were 0.96–0.14 km, 1.45–1.58 km, and 2.07–2.10 km, respectively. The results are consistent with that from the training phase.

Fig. 7 shows the density scatter plots for CERES CT models. We find that CERES CT models presented similar scatterplot distributions with MODIS cloud type CT models. Table 11 also lists the accuracies of the CERES CT models. The CT models for water-clouds2 and ice-clouds had slightly underestimated CT values with biases of −6.2E−05 – −0.16 km, and the corresponding RMSE values were 1.0,

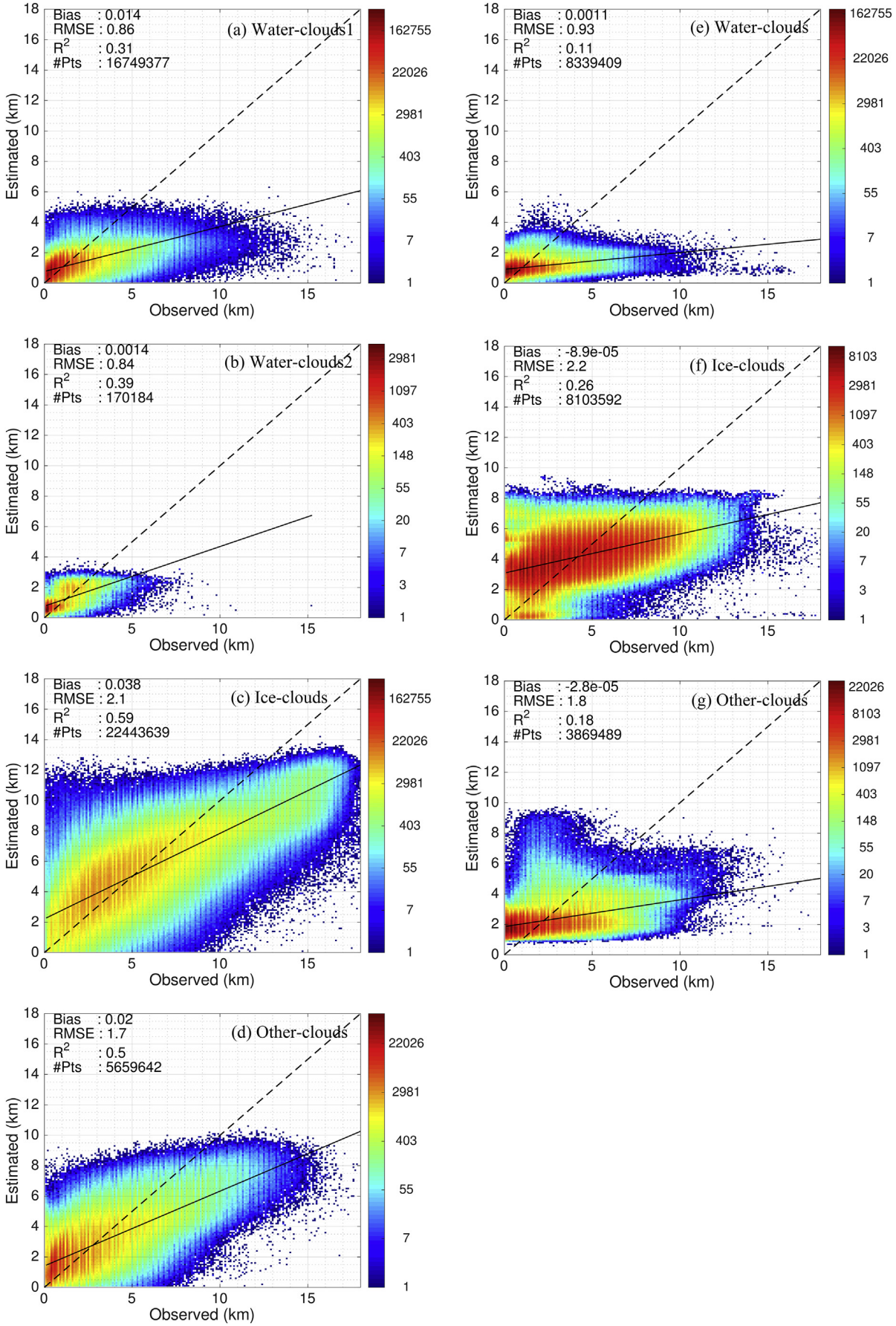

Fig. 5. Testing results of the developed CT estimation models for MODIS cloud type daytime and nighttime, respectively. The first column represents the results during daytime, and the second column represents the results during nighttime.

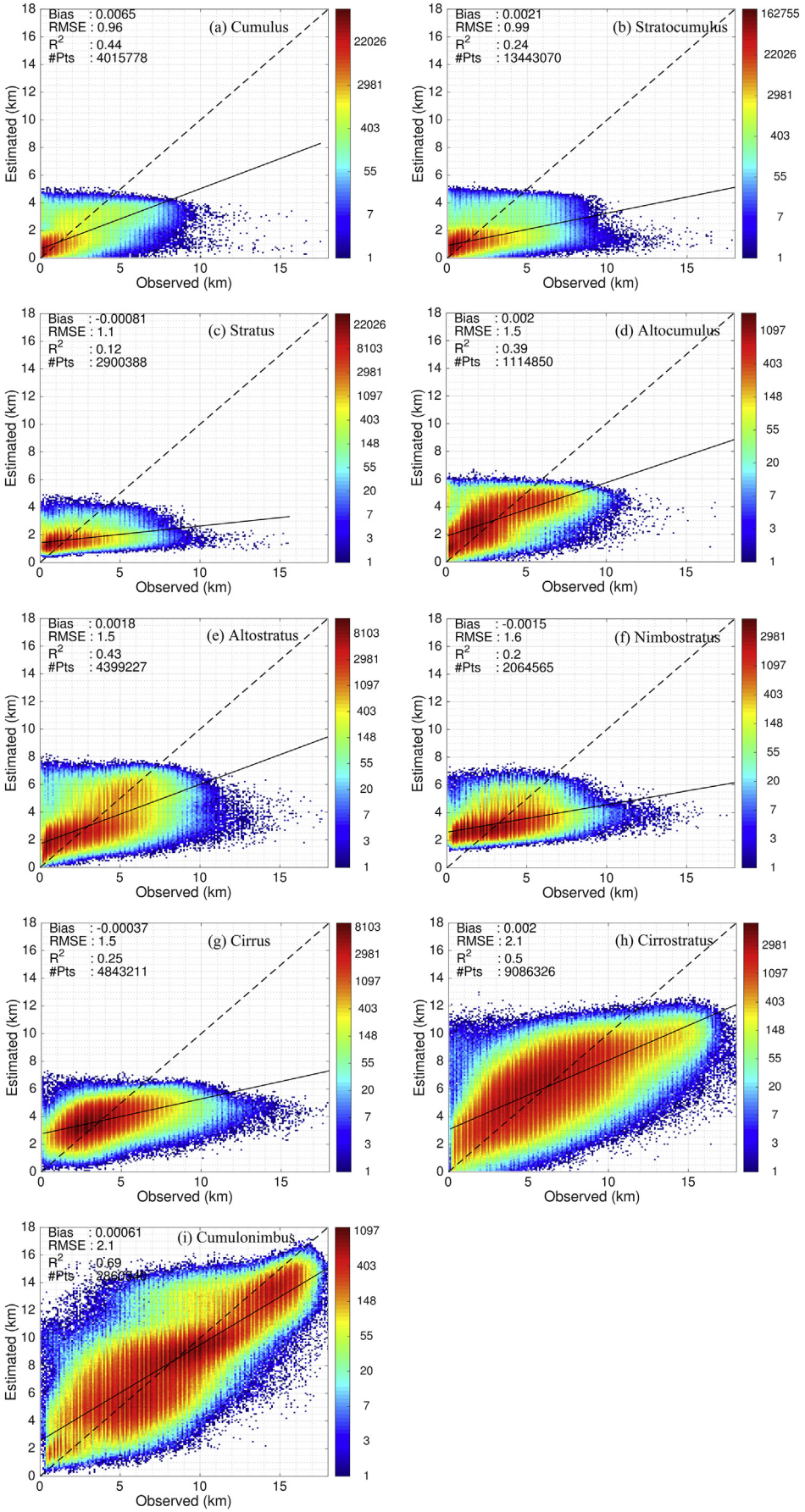

Fig. 6. Testing results of the developed CT estimation models for the ISCCP cloud type.

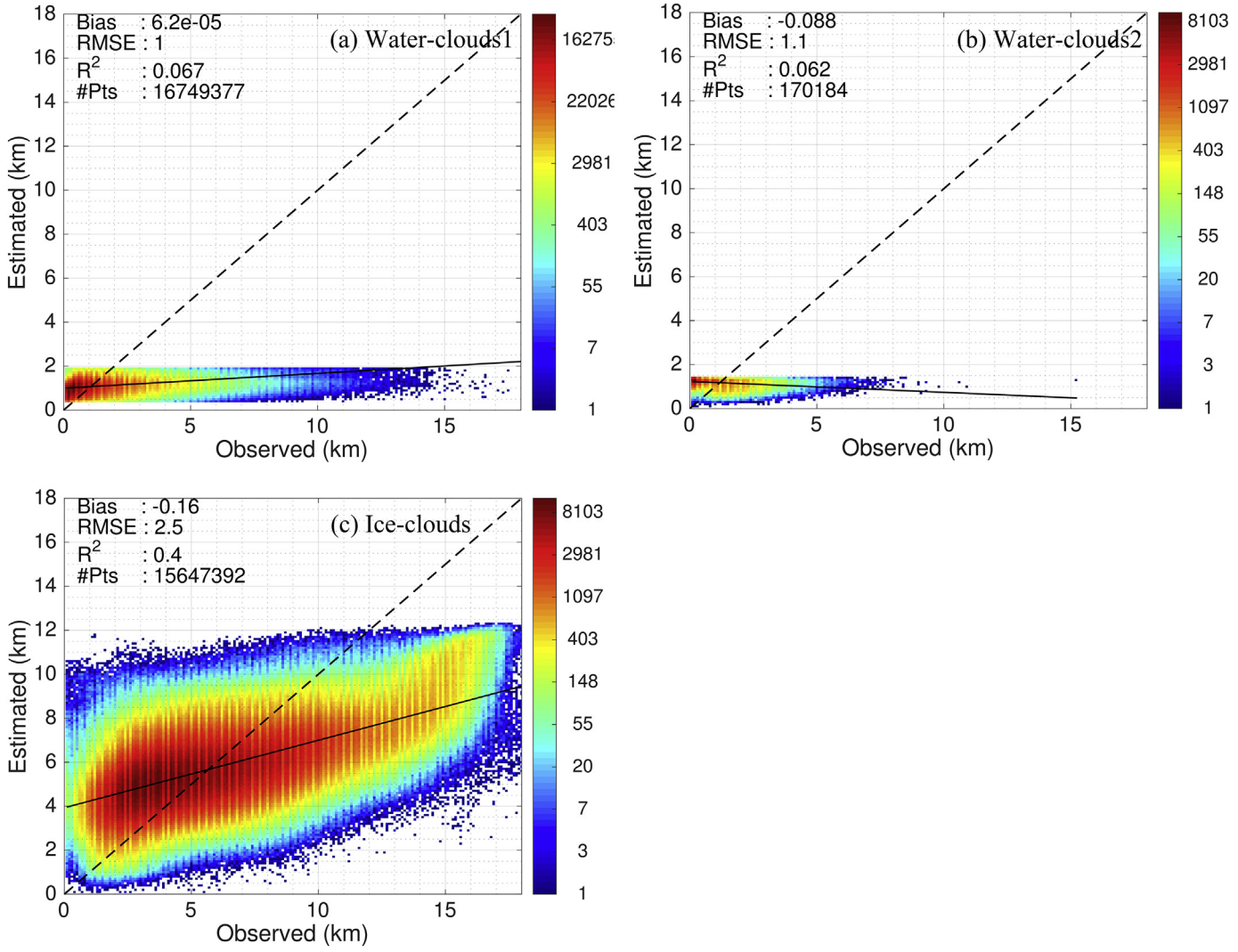

Fig. 7. The testing results of the CERES CT estimation models using the refitted coefficients.

Table 9
Testing results for the developed CT models using MODIS cloud types.

Overpass time	Cloud type	Count	RMSE (km)	bias (km)	R^2
Daytime	Water-clouds1	16,749,377	0.86	0.0138	0.31
	Water-clouds2	170,184	0.84	0.0014	0.39
	Ice-clouds	22,443,639	2.06	0.0383	0.59
	Other-clouds	5,659,642	1.67	0.0196	0.5
Nighttime	Water-clouds	8,339,409	0.93	0.0011	0.11
	Ice-clouds	8,103,592	2.21	−0.0001	0.26
	Other-clouds	3,869,489	1.75	0	0.18

Table 10
Testing results for the developed CT estimation models using the ISCCP cloud type.

Cloud level	Cloud type	Count	RMSE (km)	bias (km)	R^2
Low cloud	Cumulus	4,015,778	0.96	0.0065	0.44
	Stratocumulus	13,443,070	0.99	0.0021	0.24
	Stratus	2,900,388	1.14	−0.0008	0.12
Middle cloud	Altocumulus	1,114,850	1.52	0.0020	0.39
	Alto-stratus	4,399,227	1.50	0.0018	0.43
	Nimbostratus	2,064,565	1.58	−0.0015	0.20
High cloud	Cirrus	4,843,211	1.45	−0.0004	0.25
	Cirrostratus	9,086,326	2.07	0.0020	0.50
	Deep-convection	2,860,340	2.10	0.0006	0.69

1.15, and 2.43 km, respectively. As shown in Figs. 7(a) and (b), there seems a boundary in the estimated CTs. The cloud optical thickness (COT) was used to predict CT in the CERES CT estimate model. However, COT is retrieved from the optical and thermal infrared observations with limited penetration depth, which means the retrieved COT may by smaller than the real one. The CT derived from the lidar (CALIPSO) and radar (CloudSat) observations, which can be treated as real CT. It is reasonable to obtain smaller COT using the established relationship between real CT and the COT smaller than the real one. When more variables are incorporated into the CT predict models (e.g., Eqs. (4)–(5)), the CT estimate results are much better, please see Figs. 5(a), (b) and (e). We also compared the performance of CERES CT modes with the original and refitted coefficients. The comparison results are shown in Table 11. The CT estimation models for water-clouds1 and ice clouds using the refitting coefficients performed better than that using original coefficients. The reason may be that the refitting coefficients of CT estimate models were trained using global samples, while the original coefficients of CT estimate models were mainly trained by the observations of ARM stations. Most of the estimated CT for water-clouds2 using the original coefficients were less than 0.1 km and then set to 0.1 km based on section 3.2.3, thus we did not conduct the comparison for water-clouds2.

In summary, the density scatterplot distributions for MODIS cloud type CT models had a similar rule with the corresponding CERES CT models. Additionally, ISCCP low-level clouds, ISCCP mid-level clouds

Table 11
Comparison of CT estimate results using the original and refitted coefficients of CERES CT models.

Cloud type	Count	Original coefficients			Refitted coefficients		
		RMSE (km)	bias (km)	R^2	RMSE (km)	bias (km)	R^2
Water-clouds1	16,749,377	1	−0.23	0.08	1	6.2E−05	0.08
Water-clouds2	170,184	NA	NA	NA	1.15	−0.0880	0.06
Ice-clouds	15,647,392	3.5	−2.3	0.39	2.43	−0.1600	0.4

and ISCCP high-level cirrus clouds, and ISCCP high-level cirrostratus and cumulonimbus clouds had similar scatterplot distributions to those of MODIS water-clouds, other-clouds, and the ice-clouds CT model. Similarly, the accuracies (MODIS CT models versus CERES CT models, ISCCP CT models versus MODIS CT models) had similar values. This finding suggested that there is an internal connection for the three types of CT models.

Finally, based on training and testing performances for the ISCCP cloud type CT models, MODIS cloud type CT models, and CERES CT models, we choose the MODIS cloud type CT model or ISCCP cloud type CT model to calculate the CTs during daytime, while we only select the MODIS cloud type CT model to calculate the CTs during nighttime. We choose the CERES CT model to estimate the CTs when the CBT-based SLCM is directly used to calculate the cloudy sky SDLR without correcting the low-level cloud longwave radiation.

In addition, we need to compare the developed CT models in this study with those of similar existing studies. More specifically, MODIS cloud type CT estimates have rarely been evaluated. We conducted the validation and the results are provided in Sections 4.2.4. The comparison between the developed ISCCP cloud type CT model with the existing studies of small-scale area is conducted in section 5.1.

4.2.2. Continental, coastal and marine cloud CT estimate models

Using the same data as in Section 4.2.1, we fitted the coefficients of Eqs. (4) and (6) for land, coast and sea, and evaluated their performance. Table 12 provides the fitting results of the corresponding CT estimate models. The bias and RMSE at nighttime were smaller than those in daytime, but R^2 is on the opposite. Without considering the small difference in bias, the marine cloud CT models performed best, followed by the coastal cloud CT model and continental cloud CT models. The bias, RMSE and R^2 of the marine cloud CT models were 0.1133 km, 1.79 km, 0.67 for daytime, and 0.0259 km, 1.62 km and 0.46 for nighttime, respectively. Table 13 shows the test results of the developed cloud CT models for land, coast and sea. This result is consistent with that obtained during the fitting stage. The accuracy of the developed continental, coastal and marine cloud CT estimate models are between the performances of water clouds CT models and the ice clouds CT models in Table 9.

4.2.3. Latitudinal CT estimate models

Considering the influence of latitude on the cloud distribution, we trained and tested the CT estimate models (Eqs. (4) and (6)) for different latitudinal ranges using the same data as in Section 4.2.1. Table 14 provides the fitting results of the CT estimate models for different latitudinal ranges. In daytime, the accuracy of CT estimate is distributed symmetrically around latitudinal range 15S°-15°N, which has the highest bias, RMSE and R^2 values of 0.1909 km, 2.11 km and 0.73, respectively. The values of bias, RMSE and R^2 of other latitudinal ranges decrease gradually. We did not find such distribution during nighttime. The bias, RMSE and R^2 are less than 0.0488 km, 1.91 km and 0.54 during nighttime. Table 15 provides the testing results for the fitted CT estimate models for different latitudinal ranges. The symmetry of accuracy for different latitudinal ranges still exist in daytime. The bias and RMSE are less than 0.1916 and 2.0 km in daytime, and 0.0502 and 1.91 km during nighttime. This accuracy is comparable to the results in Sections 4.2.1 and 4.2.2.

Table 13
The testing results for the fitted CT estimate models for different surface types.

Overpass time	Surface type	Count	RMSE (km)	bias (km)	R^2
Daytime	Land	10,113,692	1.86	0.0668	0.61
	Sea	33,638,008	1.74	0.1134	0.7
	Coast	395,628	1.93	0.0506	0.6
Nighttime	Land	8,307,859	1.89	0.0091	0.31
	Sea	17,809,945	1.62	0.0251	0.47
	Coast	446,473	1.87	0.0091	0.36

4.2.4. Validation with the ARM observations

To further evaluate the developed cloud CT models, we validated the CT estimated by the developed models for MODIS cloud type with the ground measured CT. Fig. 8 shows the validation results. Most of the CTs are overestimated at SGP stations, and underestimated at NSA station. This may be caused by the difference lies in the retrieved CT and ground measured CT. The former is predicted by the cloud properties derived from the satellite observations with limited penetration depth, while the latter can represent the real CT. Table 16 provides the statistical results. The biases were − 0.6481 and 0.8935 km, and RMSE were 1.99 and 2.86 km, at NSA and SGP stations, respectively. This result is slightly poor that the test results in Section 4.2.1 (Tables 9-11), and comparable to the test results of original CERES CT model (Table 11). Using the same data, we also validated the original CERES CT models, the biases were − 0.5371 and − 2.3948 km, and RMSE are 2.07 and 3.92 km, at NSA and SGP stations. The CT estimate is improved compared to the original CERES CT models. Note the number of the collected ground measurements are too limited to guarantee the representativeness of the validation results. Thus, we will collect more ground measurement in the future to validate the developed CT estimate models.

Table 12
The fitting results of the CT estimate models for different surface types.

Overpass time	Surface type	Count	Const	Coef_cod	Coef_cer	coef_ctt	Coef_lat	Coef_cee	RMSE (km)	Bias (km)	R^2
Daytime	land	20,241,735	15.5627	0.8245	0.0957	−0.0603	−0.0220	NA	1.9	0.0666	0.58
	sea	67,332,583	16.4198	0.9382	0.1009	−0.0650	−0.0174	NA	1.79	0.1133	0.67
	coast	791,259	18.4248	0.7758	0.0907	−0.0714	−0.0142	NA	1.95	0.0485	0.58
Nighttime	land	24,725,974	19.9926	NA	NA	−0.0666	−0.0167	0.6078	1.89	0.0093	0.3
	sea	44,593,503	27.1583	NA	NA	−0.1010	−0.0292	3.4902	1.62	0.0259	0.46
	coast	1,094,207	25.2404	NA	NA	−0.0816	−0.0222	−0.2803	1.88	0.0116	0.35

Table 14
The fitting results of the CT estimate models for different latitudinal ranges.

Overpass time	Latitudinal range	Count	Const	coef_cod	coef_cer	coef_ctt	coef_lat	coef_cee	RMSE (km)	bias (km)	R^2
Daytime	75–90°N	6,724,165	26.9590	0.2267	0.0775	−0.1048	0.0089	NA	1.51	0.0066	0.54
	45–75°N	18,548,104	21.4938	0.4464	0.0751	−0.0812	−0.0056	NA	1.57	0.0422	0.65
	15–45°N	13,693,704	14.8189	1.1348	0.0955	−0.0588	−0.0271	NA	1.81	0.1407	0.67
	15S°-15°N	15,254,577	13.0725	1.7887	0.1077	−0.0580	−0.0061	NA	2.11	0.1909	0.73
	15–45°S	16,229,138	17.0895	0.9690	0.0822	−0.0660	−0.0226	NA	1.59	0.1505	0.71
	45–75°S	18,396,377	24.9616	0.2681	0.0903	−0.0936	−0.0119	NA	1.49	0.0313	0.69
	75–90°S	1,700,604	31.4925	0.1092	0.0584	−0.0966	−0.0833	NA	1.63	0.0034	0.42
Nighttime	75–90°N	12,499,867	25.3340	NA	NA	−0.0759	0.0008	−3.8196	1.91	0.0001	0.32
	45–75°N	22,622,517	30.5071	NA	NA	−0.1002	−0.0381	−3.8196	1.80	0.0215	0.47
	15–45°N	8,709,693	25.4709	NA	NA	−0.1055	−0.0235	6.6670	1.29	0.0488	0.54
	15S°-15°N	10,004,881	23.3534	NA	NA	−0.1037	−0.0145	8.3078	0.91	0.0138	0.42
	15–45°S	7,176,473	18.5590	NA	NA	−0.0736	−0.0304	4.2490	0.75	0.0176	0.35
	45–75°S	6,874,509	33.3497	NA	NA	−0.1085	−0.0516	−0.0995	1.70	0.0031	0.51
	75–90°S	4,195,579	24.2774	NA	NA	−0.0503	−0.0608	−5.1423	1.87	−3.60E-13	0.22

4.3. SDLR results

4.3.1. SDLR estimate and validation

With the developed CT estimate models, we can easily retrieve the CBT from the satellite cloud properties and reanalysis data. Then, atmospheric emissivity and atmospheric transmittance were derived using Merra-2 2 m dew point temperature and air temperature. Finally, cloudy sky SDLR were derived by SLCM provided with the estimated CBT, cloud fraction, atmospheric emissivity, atmospheric transmittance, and near-surface temperature. The CT estimated by the models developed for MODIS cloud type were used in this section because it can work during both daytime and nighttime. The SDLR estimate results using the CT derived by other models are provided in section 5.

Fig. 9 shows the scatterplot of estimated cloud sky SDLRs versus observed values at seven SURFRAD sites. Overall, the bias and RMSE of the SDLR estimates are 5.42 $W{\cdot}m^{-2}$ and 30.3 $W{\cdot}m^{-2}$, respectively. During daytime, the bias and RMSE of SDLR estimates are 11.4 $W{\cdot}m^{-2}$ and 30.8 $W{\cdot}m^{-2}$, respectively. During nighttime, the SDLR estimate had a bias and RMSE of 1.95 $W{\cdot}m^{-2}$ and 30 $W{\cdot}m^{-2}$, respectively. This finding suggested that the SDLR estimate during daytime had an obvious overestimation phenomenon that was likely because of an inappropriate low-level cloud upper boundary used to correct the corresponding cloud longwave radiation. Fig. 10 provides a comparison of the low-level cloudy sky SDLR estimates before and after correcting the corresponding cloud longwave radiation. We find that the SDLR estimates before correcting the low-level cloud longwave radiation were seriously overestimated with a bias and RMSE of 32.9 $W{\cdot}m^{-2}$ and 44.5 $W{\cdot}m^{-2}$, respectively, whereas the bias and RMSE are −3.85 $W{\cdot}m^{-2}$ and 30.1 $W{\cdot}m^{-2}$, respectively, after correcting the low-level cloud longwave radiation. This finding suggested that the SDLR estimate with correcting low-level cloud longwave radiation can obviously improve the accuracy of the SDLR estimate in the CBT-based SLCM.

Finally, in Table 17, we counted the accuracy of the SDLR estimates at seven SURFRAD sites. The biases and RMSEs of the SDLR estimates ranged from 3.56 to 11.24 $W{\cdot}m^{-2}$ and 25.11 to 30.82 $W{\cdot}m^{-2}$, respectively with the exception of the DRA site and TBL site. During daytime, the SDLR estimates had bias accuracies of 3.56–11.24 $W{\cdot}m^{-2}$ and RMSEs of 24.85–31.44 $W{\cdot}m^{-2}$ except for the DRA and TBL sites. During nighttime, the SDLR estimates had biases of −0.61-9.14 $W{\cdot}m^{-2}$ and RMSEs of 25.26–30.47 $W{\cdot}m^{-2}$ except for the DRA site and TBL site. This finding suggested that the SDLR estimates at the DRA site and TBL site had relatively worse accuracy, which was caused by the fact that the DRA site was located in a rugged area, and the TBL had a larger surface elevation.

4.3.2. Comparison with existing studies

As shown in Table 18, total comparisons of SDLR estimates with the existing works (Gui et al., 2010Wang et al., 2018Yu et al., 2018) were conducted in this study. This is explained by the fact that: (1) There are few studies that estimate high-resolution all-sky SDLR in the literature. The mainstream SDLR products are GEWEX-SRB, ISCCP-FD and CERES-FSW SDLR products, but their spatial resolutions are really coarse. Moreover, Gui et al. (2010) have conducted comprehensive evaluation of these three products with ground measurements. (2) Our study is similar to Wang et al. (2018) and Yu et al. (2018). We all used the single layer cloud model. The differences are that Wang et al. (2018) developed the method of integrating AIRS and AMSR-E temperature and moisture profiles, and calculated the CBT from satellite CTH product and CT derived by the CERES CT model; Yu et al. (2018) derived the CBT from the temperature profile of reanalysis product, and calculated the CBT from satellite CTH product and CT derived by the CERES CT model; and we developed the global CT estimate model, derived the CBT from the temperature profile of reanalysis product, satellite derived CTH product and estimated CT.

In cloudy sky conditions, the SDLR estimates in this study had the smallest bias with a value of 5.42 $W{\cdot}m^{-2}$ and the lowest RMSE of 30.3 $W{\cdot}m^{-2}$, with the exception of the SDLR estimate for CERES-FSW with an RMSE of 22.9 $W{\cdot}m^{-2}$. We also compared the SDLR estimate with the existing studies in all sky conditions (Table 18), which was considered because of the validation sites were almost the same. The bias in our study was smaller than the SDLR estimate from ISCCP-FD

Table 15
The testing results for the fitted CT estimate models for different latitudinal ranges.

Latitudinal range	Overpass time	Count	RMSE (km)	bias (km)	R^2	Overpass time	Count	RMSE (km)	Bias (km)	R^2
75–90°N	Daytime	3,359,565	1.51	0.0091	0.54	Nighttime	4,580,700	1.91	−0.0024	0.32
45–75°N		9,267,225	1.55	0.0415	0.66		9,601,575	1.79	0.0211	0.48
15–45°N		6,849,236	1.74	0.1414	0.71		3,063,424	1.26	0.0502	0.57
15S°-15°N		7,622,930	2.00	0.1916	0.77		3,406,886	0.90	0.0138	0.44
15–45°S		8,104,698	1.51	0.1499	0.75		2,695,261	0.73	0.0173	0.38
45–75°S		9,186,325	1.48	0.0312	0.70		2,822,418	1.69	0.0019	0.51
75–90°S		849,353	1.62	0.0032	0.42		1,051,407	1.87	0.0001	0.22

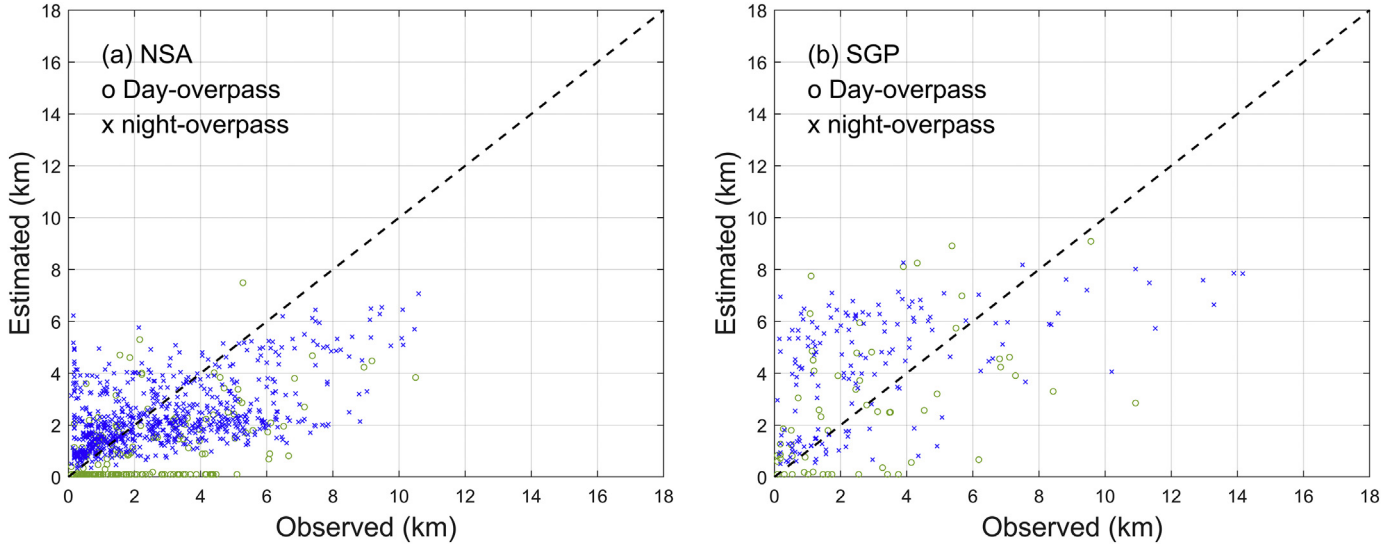

Fig. 8. Scatterplots of estimated and observed CTs at ARM NSA and SGP stations.

Table 16
Validation results of the developed CT models for MODIS cloud type at ARM NSA and SGP stations.

Station	Overpass time	Count	Bias (km)	RMSE (km)
NSA	day	211	−1.1526	2.04
	night	776	−0.5109	1.98
	all	987	−0.6481	1.99
SGP	day	58	−0.0231	2.68
	night	159	1.2279	2.93
	all	217	0.8935	2.86

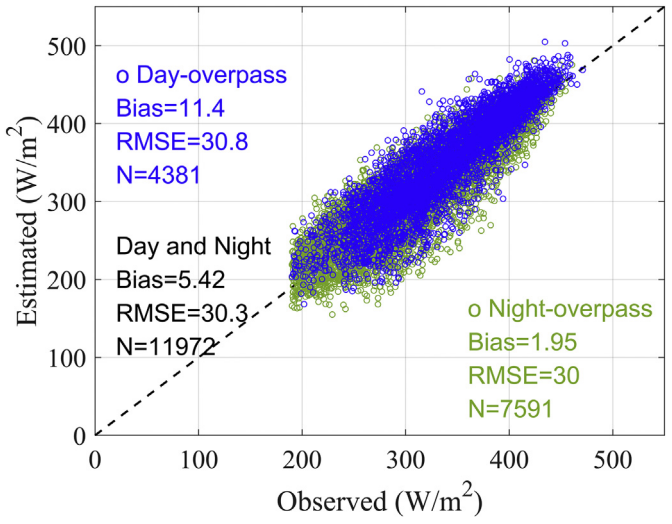

Fig. 9. Validation results of estimated cloudy sky SDLRs at seven SURFRAD sites.

and CERES-FSW, with the exception of the SDLR estimate from GEWEX-SRB. Our study had the lowest RMSE, with the exception of the SDLR estimate from CERES-FSW with an RMSE of 18.5 W·m^{-2}. This is possibly because the SDLR estimate performances from GEWEX-SRB, ISCCP-FD and CERES-FSW included clear sky evaluations, but the clear sky SDLR estimate generally yielded a higher accuracy (Cheng et al., 2017). Regarding the SDLR estimate in all sky conditions, the accuracy of our work is no lower than that for most of the existing studies, although our study did not yield the best accuracy.

Moreover, Fig. 11 shows site-by-site comparisons of the SDLR estimates in this study with those of the existing studies. All studies had relatively larger biases at the DRA site (the rugged area) and TBL site (the larger surface elevation). The bias of our work at other sites had a relatively smaller difference from the existing studies with a bias of less than 11.24 W·m^{-2}. Our study had relatively lower RMSE with the exception of the DRA site and TBL site, but the RMSEs of our work at the DRA site and TBL site were slightly larger than those of the existing studies. This finding suggested that our work can achieve an acceptable accuracy regarding site-by-site SDLR validation. Note that our study showed a preliminarily improvement in the overestimation phenomenon of the SDLR estimate using CBT-based SLCM, but validation studies were still required. For example, the SDLR estimate at the larger surface elevation TBL site can be directly estimated and verified with biases of 7.22 W·m^{-2} and 25.7 W·m^{-2}.

Overall, our study can achieve a satisfactory accuracy with a bias of 5.42 W·m^{-2} and RMSE of 30.3 W·m^{-2}, compared to the existing SDLR estimate accuracy from methods of SDLR estimates or products (GEWEX-SRB, ISCCP-FD and CERES-FSW). Additionally, the SDLR estimate in this study can produce SDLRs with a 5-km spatial resolution during both daytime and nighttime. However, in the future, we need to conduct an SDLR estimate with a larger surface elevation location.

4.3.3. The relationship between SDLR and its affecting variables

We quantitatively analyzed the contributions (in terms of the determination coefficient, R^2) of COT, CBT, TPW, T2M (2 m air temperature), and E2M (clear air emissivity) to the measured cloud sky SDLR at SURFRAD network. The matched COT, CBT, TPW, T2M, and E2M samples were obtained from section 4.3.1. CBT, T2M, and E2M are the inputs to SLCM, while COT and TPW have significant impacts on SDLR. Fig. 12 shows the scatterplots between the abovementioned parameters and site measured SDLRs when dividing all samples into daytime and nighttime parts. R^2 of the atmospheric parameters is larger than 0.64, while the R^2 of the CBTs were 0.12 and 0.077 during daytime and nighttime, respectively. There is a scatter separation phenomenon between the TPW and observed cloudy sky SDLR, which may be caused by that TPW has relatively larger elevation difference between the six SURFRAD sites (i.e., BND, DRA, FPK, GWN, and PSU) and TBL site.

TPW can explain a considerable part (approximately 68%) of SDLR, while the contribution of CBT is less than 8%. Combine the results of sensitivity analysis, we attempted to predict cloudy sky SDLR with TPW and CBT. With the randomly selected two-thirds of the samples that were used in section 4.3.1, we fit the nonlinear relationship between

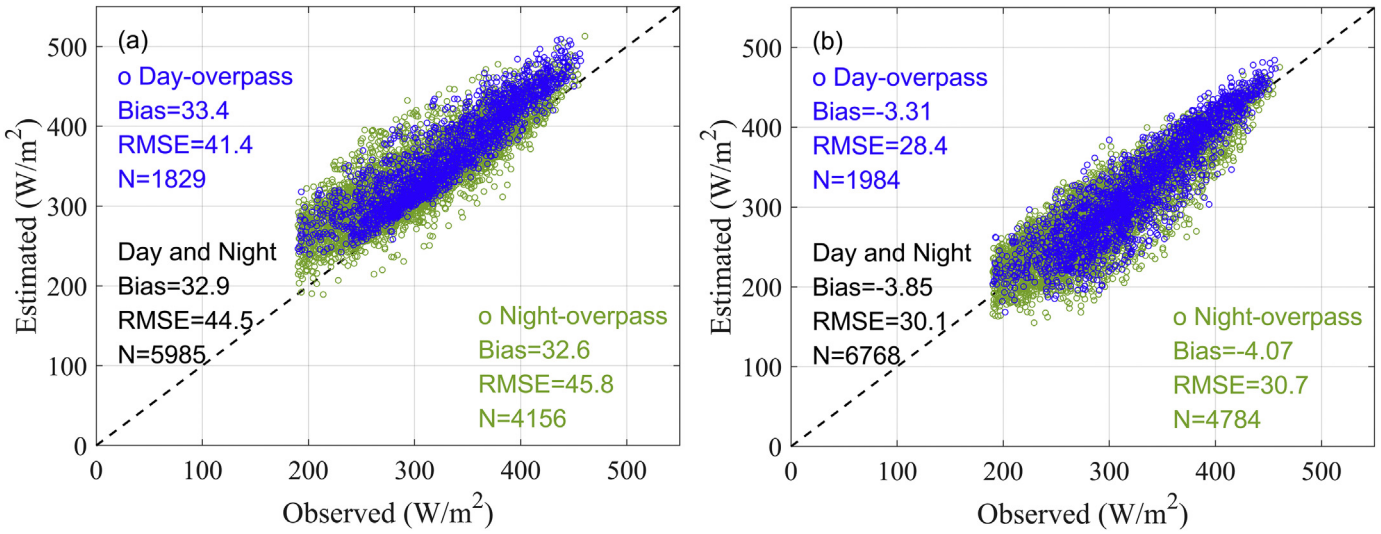

Fig. 10. Validation results of estimated low-level cloudy sky SDLRs before (a) and after (b) correcting their low-level cloud longwave radiation reaching surface.

SDLR and TPW and CBT. The fitted formula is shown as Eq. (16). The remaining one-third of samples were used to test the fitted formula, and the tested results are show in Fig. 13. It is clear that the proposed hybrid method performed well, with an RMSE of 33.9 W·m^{-2} and bias of 0.681 W·m^{-2}.

$$SDLR = 269.84 + 58.70TPW - 0.08lnCBT \quad (16)$$

5. Discussion

5.1. CT retrieval at the global scale

This study first constructed a cloud property database at the global scale, including 135,820,004 and 108,125,279 data points during daytime and nighttime, respectively; thus, this database is very representative and can be used to developed CT estimate models. Additionally, the chosen factors that predict CT have very clear physical meanings (Platnick et al., 2003), and they all have relatively stronger physical relationships with CT (Chakrapani et al., 2002Minnis et al., 2011Minns et al., 1992). This can improve stability of the developed CT models. Importantly, this study introduced the latitude variable to regulate the temperature and water vapor variabilities from the poles to the equator, which greatly affects cloud properties (Miller et al., 2014). Finally, this study established relationships among the ISCCP cloud type CT estimate, MODIS cloud type CT estimate, and CERES CT estimate, which may provide potential choices for different users. Overall, the developed CT models achieved a satisfactory accuracy based on the training and testing results.

However, the CT used in this study is the sum of the CTs of multiple layer clouds, so the inversed CT may be less than the real CT value if there is a gap between two layers of clouds. Therefore, larger uncertainty may exist in the derived SDLR when this phenomenon occurs. A large number of samples were used to develop the CT estimate model, and the MLR method was adopted, which allowed for simplicity. Later, we will attempt to use the complex methods (Chakrapani et al., 2002Rao et al., 2019).

We attempted to compare the accuracies of the CT estimate results in this study with those of similar studies. However, we did not find similar studies for MODIS cloud type in the literature. Therefore, we compared the ISCCP cloud type CT estimates in this study to those of the existing studies conducted at local scales (Chakrapani et al., 2002Minnis et al., 1990aMinns et al., 1992), whose accuracy are presented in Table 19. Note that the cloud properties used to predict CTs are different. The cloud types are the same (cumulus, stratocumulus, stratus, and cirrus). Generally, the bias of the estimated CT is extremely low, and the existing studies did not provide biases of their estimated CTs with the exception of cirrus. Regarding cirrus, our accuracy is much better. The RMSEs of the estimated CTs are larger than those of the existing studies with the exception of cumulus. The potential reason is that the developed CT estimate model is a global model, whereas existing studies used local models that were developed and tested by tens or hundreds of samples. Thus, we believe our CT estimate accuracy is comparable to those of existing studies conducted at local scales.

5.2. SDLR retrieval using different sources of CBT

The SLCM framework has been established for a long time (Diak et al., 2000Gupta et al., 2010Kimball and Idso, 1982Schmetz et al., 1986Wang et al., 2018). The research hotspot focuses on how to derive CBT, which dominates the accuracy of cloud sky SDLR estimates using SLCM (Bisht and Bras, 2010Diak et al., 2000Gupta et al., 2010Kimball and Idso, 1982Schmetz et al., 1986Wang et al., 2018). Here, we investigated the effects of MODIS CTT and three types of estimated CBTs (i.e., ISCCP CBT, MODIS CBT, and CERES CBT) on SDLR estimates using SLCM. The method of deriving ISCCP and CERES CBTs were the same as that used to derive MODIS CBT, which is discussed in detail in section

Table 17
Validation results of the cloudy sky SDLRs at seven SURFRAD sites.

Accuracy index	Overpass time	BND	DRA	FPK	GWN	PSU	SXF	TBL	All sites
bias (W·m^{-2})	day and night	6.98	27.57	11.24	8.32	3.56	8.61	−17.3	5.42
	day	10.84	37.72	14.96	13.90	10.10	13.89	−8.76	11.4
	night	4.56	22.21	9.14	5.20	−0.61	5.48	−21.5	1.95
RMSE (W·m^{-2})	day and night	25.51	39.49	30.82	25.11	26.08	28.85	38.3	30.3
	day	25.39	48.13	31.44	24.85	25.65	28.70	38	30.8
	night	25.58	34.05	30.47	25.26	26.34	28.94	38.4	30

Table 18
Comparisons of SDLR estimates in this study with existing studies.

Author	Method or product	Weather types	Sites	Bias ($W{\cdot}m^{-2}$)	RMSE ($W{\cdot}m^{-2}$)
This study	CBT-based SLCM	cloudy sky	seven SURFRAD sites	5.42	30.3
Gui et al. (2010)	GEWEX-SRB product	cloudy sky	fifteen sites from SURFRAD, CEOP-Tibet, and AsiaFlux	5.8	32
	ISCCP-FD product	cloudy sky		10	35.2
	CERES-FSW product	cloudy sky		−11.8	22.9
	GEWEX-SRB product	all sky	six SURFRAD sites except for SXF site	0.1	32.7
	ISCCP-FD product	all sky		9.7	35.8
	CERES-FSW product	all sky		−8.8	18.5
Wang et al. (2018)	CBT-based SLCM product	cloudy sky	seven SURFRAD sites	−7.7	32.8
Yu et al. (2018)	CBT-based SLCM (Schmetz et al., 1986)	cloudy sky	eleven sites from networks of HiWATER, ARM, and BSRN	21.7	42.5
	CBT-based SLCM (Gupta et al., 2010)	cloudy sky		15.9	33.3
	CBT-based SLCM (Diak et al., 2000)	cloudy sky		24.3	41.8

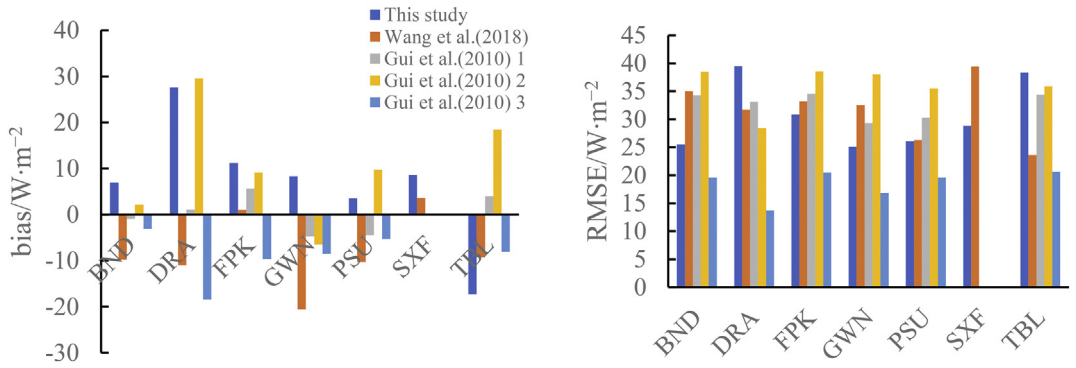

Fig. 11. The site-by-site comparisons of SDLR estimates between this study and the existing studies at seven SURFRAD sites. Note that this study and Wang et al. (2018) evaluated cloudy sky SDLRs, while Gui et al. (2010) evaluated all sky SDLRs. Gui et al. (2010) 1, Gui et al. (2010) 2, and Gui et al. (2010) 3 were all sky SDLR evaluation accuracies for GEWEX-SRB, ISCCP-FD, and CERES-FSW, respectively.

4.3.1.

Fig. 14 shows the histograms of the aforementioned estimated CBTs. The mean values for MODIS CBT, CERES CBT, ISCCP CBT, and MODIS CTT were 280 K, 246 K, 266 K, and 252 K, respectively; during daytime, the mean MODIS CBT was 266 K, while at nighttime, the mean MODIS CBT was 252 K; CERES CBT and MODIS CTT both had two peak values. MODIS CBT and ISCCP CBTs had relatively smaller standard deviations (stds) than CERES CBT and MODIS CTT, whose std. values ranged from 13.2–13.5 K to 24.6–27.2 K. Additionally, MODIS CBT and ISCCP CBT are mainly larger than 240 K; CERES CBT and MODIS CTT have bimodal distributions and both range from 210 to 300 K. This may suggest that the temporal variability in CERES CBT is similar to that of MODIS CTT.

Table 20 provided the comparison results of the SDLR estimate using three CBT-based SLCMs and CTT-based SLCM at SURFRAD sites. During daytime, the bias and RMSE of SDLR estimates using CBT were all better than that estimated by CTT, with the exception of the SDLR estimated by MODIS CBT, whose bias was slightly larger than that of the CTT estimated SDLR. For example, the SDLR estimate using CERES CBT had a bias of 0.54 $W{\cdot}m^{-2}$ and RMSE of 25 $W{\cdot}m^{-2}$, while the bias and RMSE of the SDLR estimate with MODIS CTT were 11.5 $W{\cdot}m^{-2}$ and 31.3 $W{\cdot}m^{-2}$, respectively. During nighttime, the bias and RMSE of the SDLR estimated using MODIS CBT were better than that estimated by CTT, with values of 1.95 and 30 $W{\cdot}m^{-2}$ and 11.5 and 37.5 $W{\cdot}m^{-2}$, respectively. The total accuracies of the SDLR estimated by MODIS CBT were 5.42 $W{\cdot}m^{-2}$ (bias) and 30.3 $W{\cdot}m^{-2}$ (RMSE), compared with the SDLR estimated by MODIS CTT, with a bias of 11.5 $W{\cdot}m^{-2}$ and RMSE of 35.4 $W{\cdot}m^{-2}$. Clearly, the physically based CBT can improve the accuracy of cloudy sky SDLR estimates better than that of directly using the CTT in the SLCM.

6. Conclusions

CBT is an important parameter that dominates the cloudy sky SDLR. However, the satellite CBT product has rarely been available at regional and global scales, which limits the application of CBT in the estimates of cloud sky SDLR. In this study, a framework for estimating global cloudy sky SDLR in both daytime and nighttime was developed. First, we constructed the cloudy property database by combing the CVS parameters from CloudSat and cloud property parameters from MODIS. Then, the empirical models for estimating CT and CBT under the ISCCP cloud classification system and MODIS cloud classification system were developed. With the constructed database, we also refitted the coefficients of the CERES CT estimate models, which were originally determined by data at the local scale. With the estimated CT and reanalysis data, it is straightforward to calculate the corresponding CBT. Finally, the cloudy sky SDLR were obtained by inputting the estimated CBT and other parameters into the SLCM.

The training, testing and validation results of the developed CT models for MODIS cloud type are in good consistent. We did not find similar studies of CT estimate for ISCCP cloud type in the literature. Thus, we compared the accuracies of the CT estimation results in this study with those of similar studies that were conducted at local scales (Chakrapani et al., 2002Minnis et al., 1990aMinns et al., 1992). Generally, the bias of the estimated CT is extremely low, while the existing studies did not provide the biases of their estimated CTs with the exception of cirrus. Regarding cirrus, our accuracy is much better. The RMSEs of estimated CTs are larger than those of the existing studies with the exception of cumulus. The potential reason is the developed CT estimate model is a global model, and the existing studies used a local model that was developed and tested by tens or hundreds of samples. Thus, we believe our CT estimate accuracy is comparable to the existing studies conducted at local scales.

The SLCM estimated cloudy sky SDLR are validated by the ground

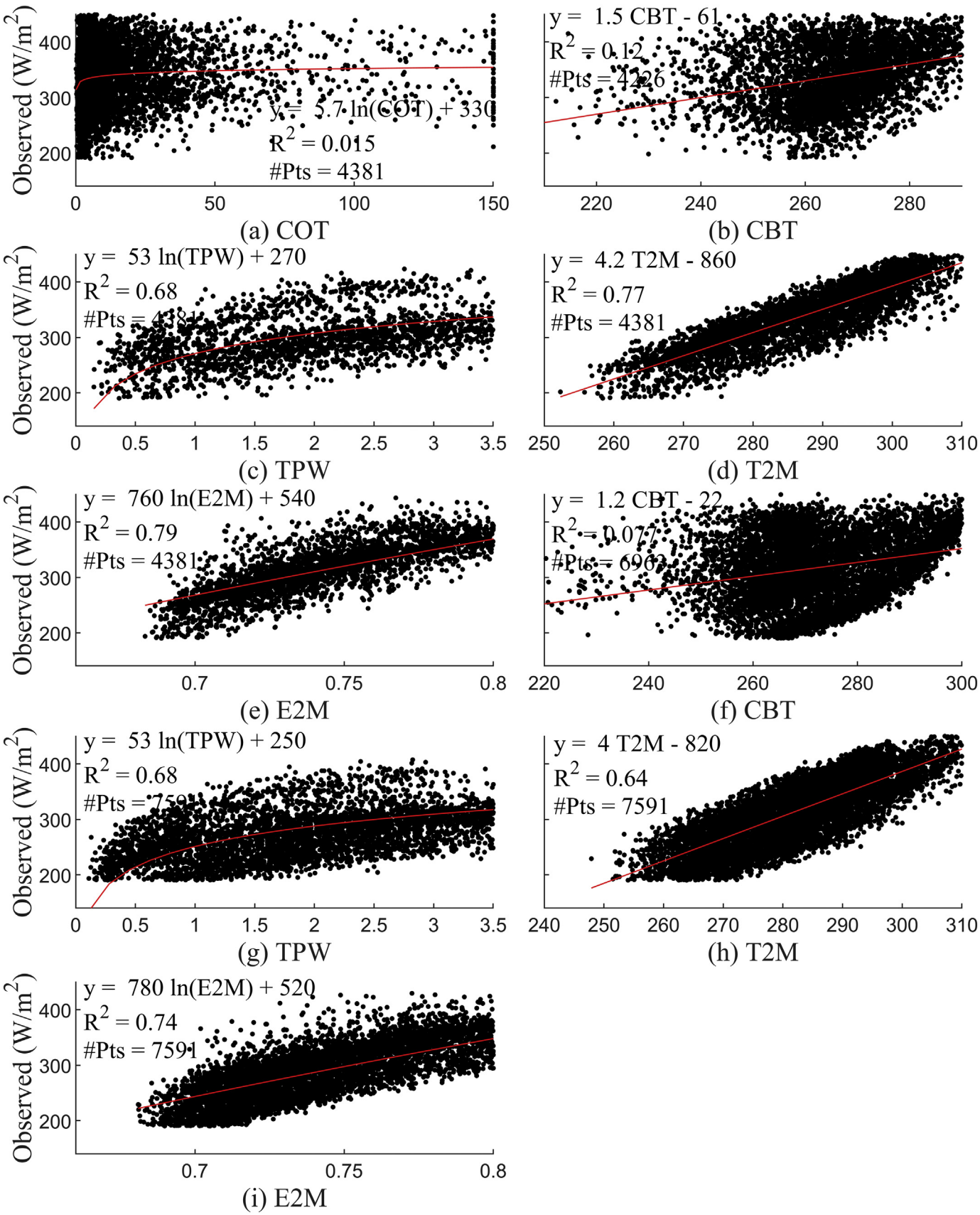

Fig. 12. The contributions of COT, CBT, TPW, T2M, and E2M to measured cloudy sky SDLR for all samples. The subplots (a)-(e) are the results for daytime, and subplots (f)-(i) are the results for nighttime.

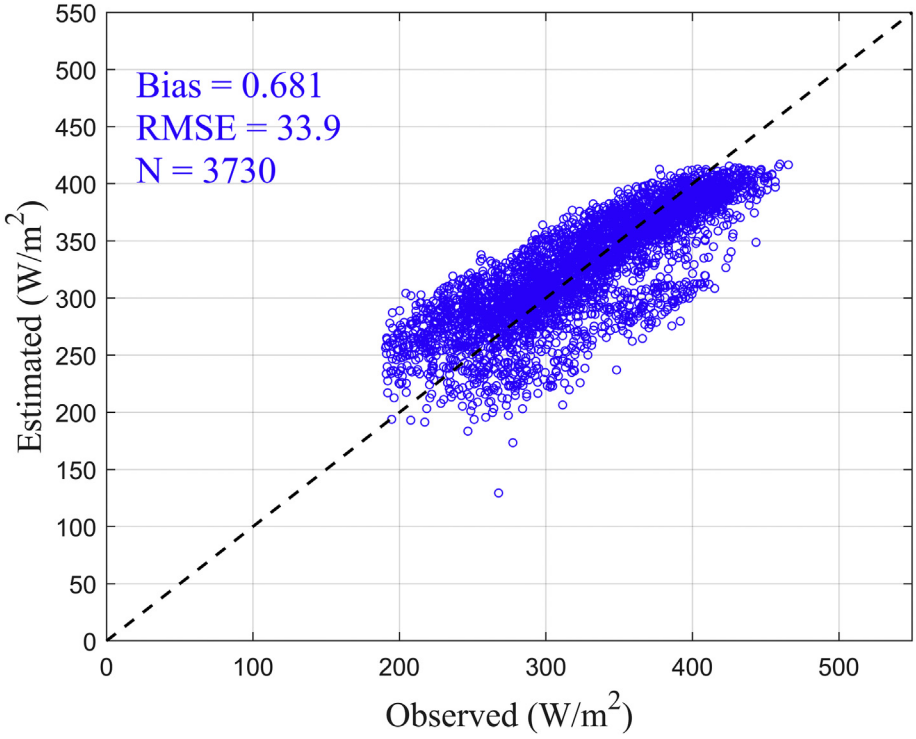

Fig. 13. The testing results of the proposed hybrid method for estimating the cloudy sky SDLR.

measured SDLR collected from the SURFRAD network. The bias and RMSE are 5.42 W·m^{-2} and 30.3 W·m^{-2}, respectively. The accuracy of this study is comparable to the evaluation results of the mainstream GEWEX-SRB, ISCCP-FD and CERES-FSW products, the evaluation results of Yu et al. (2018), and the validation accuracy of the method of Wang et al. (2018). The merit of this study is that the developed framework can be used to estimate 5-km SDLR during both daytime and nighttime. When compared to the SLCM that directly uses CTT, the physical-based CBTs derived using three cloud type classification systems all improve the cloudy sky SDLR estimate accuracy.

There are some limitations worth noting that need to be improved in the future: (1) The impact of the cloud type classification system. According to the evaluation results of the estimated CT in section 4.2, the accuracies of the CT estimates under different cloud type classification systems are different, which will inevitably affect the accuracies of the estimated CBT and SDLR. (2) The uncertainties in the measured CTs with complex CVSs. CT, as dependent variable input, was the sum of the sub CTs from multiple layer clouds. The retrieved CT may be less than the real CT value if there is a gap between the two layers of clouds. In addition, the used cloud properties are only measured in a certain range below the cloud top. (3) The correction of SDLR for low-level cloud type. The pressure difference between the surface and the CBP is set to 320 hPa, although this study has modified the low-level cloud sky SDLR. In fact, this is the reference value of Gupta et al. (1992) and Doutriaux-Boucher and Sèze (1998). In future research, a more reasonable pressure difference threshold should be experimentally determined. (4) Validation of estimated CT and SDLR. We will collect more ground measurements of CT and SDLR to comprehensively validate the developed CT-estimated method and the SLCM-estimated SDLR in the future.

Author Statement

Jie Cheng: Conceptualization, Methodology, Supervision, Reviewing and Editing.

Feng Yang: performed the experiments, analyzed the data and prepared the original draft.

Declaration of Competing Interest

The authors declare that they have no known competing financial interests or personal relationships that could have appeared to influence the work reported in this paper.

Acknowledgement

This work was partly supported by the National Natural Science Foundation of China via grant 41771365, the National Key Research and Development Program of China via grant 2016YFA0600101 and the National Natural Science Foundation of China via grant 41371323.

Table 19
The accuracy of the existing CT estimation studies for ISCCP cloud type for small-scale areas.

Author	Location	Cloud type	Bias (W·m^{-2})	RMSE (W·m^{-2})	Count	Cloud properties
Minnis et al. (1990a)	FIRE	cirrus	0.29(−0.0004)	1(1.45)	NA	T_c, COT, σ_a (CEE, CER, CTT, and latitude)
Minns et al. (1992)	southwest of Los Angeles	stratocumulus	NA (0.0021)	0.06(0.99)	NA	COT (CEE, CER, CTT, and latitude)
Chakrapani et al. (2002)	ARM-SGP	cirrus	NA (−0.0004)	0.84(1.45)	65	σ(Tc), CER, COT (CEE, CER, CTT, and latitude)
		cumulus	NA (0.0065)	1.26(0.96)	141	COT (CEE, CER, CTT, and latitude)
		thick stratus	NA (−0.0008)	0.61(1.14)	209	σ(Tc), COT (CEE, CER, CTT, and latitude)
		thin stratus	NA (−0.0008)	0.35(1.14)	208	NA (CEE, CER, CTT, and latitude)

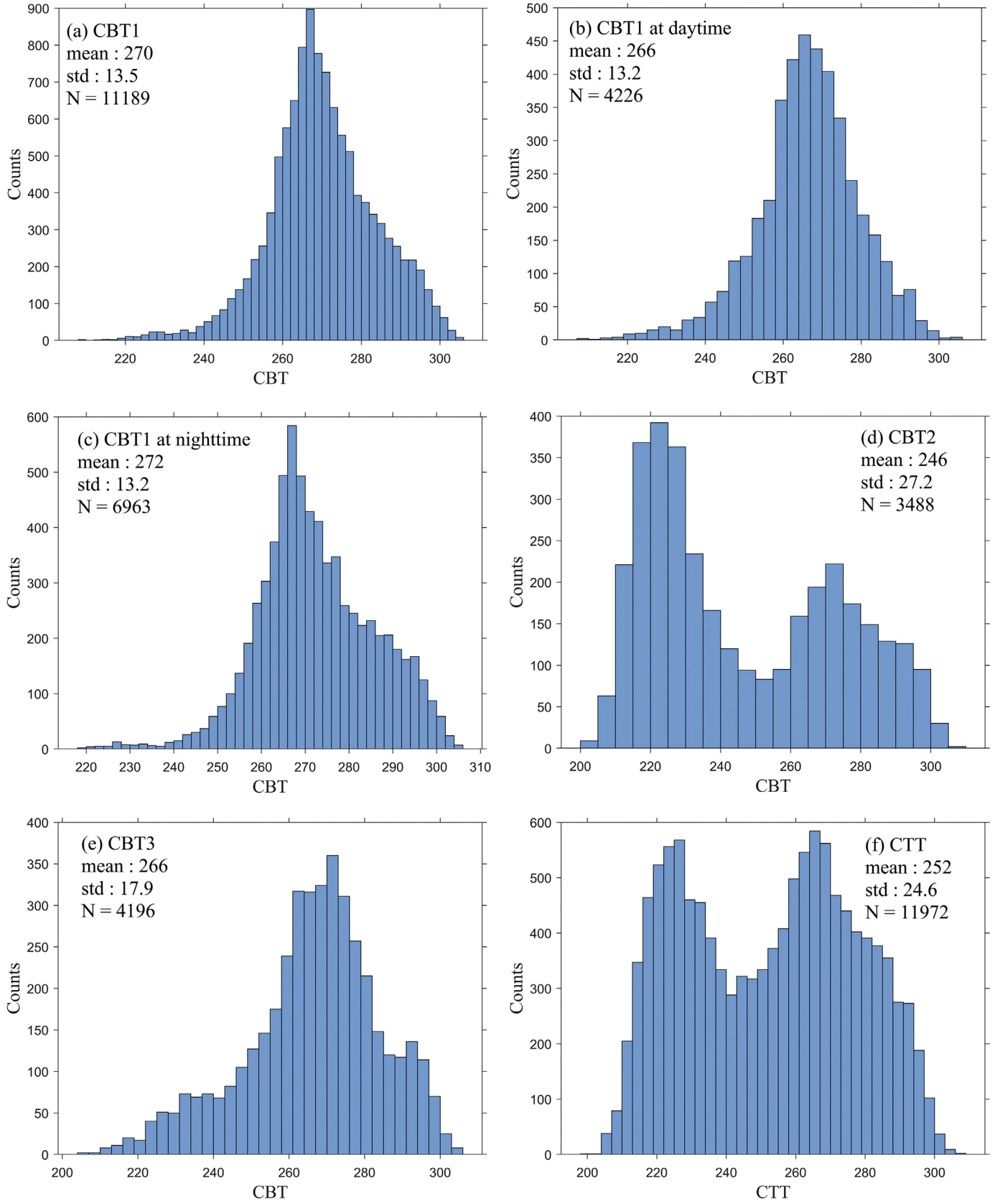

Fig. 14. Histograms of MODIS CTT and three categories of CBTs estimated by combining MODIS CTH, Merra-2 temperature profile, and CT estimated from the CT models in section 4.2. (CBT1, CBT2, and CBT3 were derived from MODIS CT, CERES CT, and ISCCP CT, respectively, while CTT was provided by MYD06).

Table 20
Evaluation of cloudy sky SDLRs estimated by MODIS CTT and three types of estimated CBTs with SURFRAD site measurements.

Cloud temperature	Overpass time	Bias ($W{\cdot}m^{-2}$)	RMSE ($W{\cdot}m^{-2}$)	Number of samples
MODIS CBT	Day + Night	5.42	30.3	11,972
	Day	11.4	30.8	4381
	Night	1.95	30	7591
CERES CBT	Day	0.54	25	3513
ISCCP CBT	Day	3.99	30.4	4381
MODIS CTT	Day + Night	11.5	35.4	11,972
	Day	11.5	31.3	4381
	Night	11.5	37.5	7591

References

Ackerman, S., Frey, R., Strabala, K., Liu, Y., Gumley, L., Baum, B., Menzel, P., 2010. Discriminating clear-sky from cloud with MODIS algorithm theoretical basis document (MOD35) Version 6.1. Cooperative Institute for Meteorological Satellite Studies. University of Wisconsin—Madison, Madison, WI, USA. https://modis-images.gsfc.nasa.gov/_docs/MOD35_ATBD_Collection6.pdf.

Augustine, J.A., DeLuisi, J.J., Long, C.N., 2000. SURFRAD–A national surface radiation budget network for atmospheric research. Bull. Am. Meteorol. Soc. 81, 2341–2358.

Barker, H.W., Jerg, M.P., Wehr, T., Kato, S., Donovand, D.P., Hogan, R.J., 2011. A 3D cloud-construction algorithm for the EarthCARE satellite mission. Q. J. R. Meteorol. Soc. 137, 1042–1058.

Barkstrom, B.R., 1984. The earth radiation budget experiment (ERBE). Bull.amer.meteor.sci 65, 1170–1185.

Berk, A., Bernstein, L.S., Robertson, D.C., 1989. MODTRAN: A moderate resolution model for LOWTRAN. Final Report GL-TR-89-0122, Geophysics Laboratory, U.S. Air Force Systems Command, Hanscomb AFB, Massachusetts, USA.

Bisht, G., Bras, R.L., 2010. Estimation of net radiation from the MODIS data under all sky conditions: southern Great Plains case study. Remote Sens. Environ. 114, 1522–1534.

Bisht, G., Bras, R.L., 2011. Estimation of net radiation from the moderate resolution imaging Spectroradiometer over the continental United States. IEEE Trans. Geosci. Remote Sens. 49, 2448–2462.

Bréon, F.-M., Frouin, R., Gautier, C., 1991. Downwelling longwave irradiance at the ocean surface: an assessment of in situ measurements and parameterizations. J. Appl. Meteorol. 30, 17–31.

Carmona, F., Rivas, R., Caselles, V., 2014. Estimation of daytime downward longwave radiation under clear and cloudy skies conditions over a sub-humid region. Theor. Appl. Climatol. 115, 281–295.

CEOS, & WMO, 2000. CEOS/WMO Online Database: Satellite System and Requirements in. The Committee on Earth Observation Satellites, The World Meteorological Organization.

Chakrapani, V., Doelling, D.R., Rapp, A.D., Minnis, P., 2002. Estimation.Cloud thickness.GOES-8_satellite.ARM-SGP Site. In: Twelfth ARM Science Team Meeting Proceedings, pp. 8–12.

Cheng, J., Liang, S., Wang, W., Guo, Y., 2017. An efficient hybrid method for estimating clear-sky surface downward longwave radiation from MODIS data. J. Geophys. Res.-Atmos. 122, 2616–2630.

Cheng, J., Liang, S., Wang, W., 2018. Surface Downward Longwave Radiation. *Comprehensive Remote Sensing*. Elsevier, Oxford, pp. 196–216.

Cheng, J., Yang, F., Guo, Y., 2019. A comparative study of bulk parameterization schemes for estimating cloudy-sky surface downward Longwave radiation. Remote Sens. 11, 528.

Crawford, T.M., Duchon, C.E., 1999. An improved parameterization for estimating effective atmospheric emissivity for use in calculating daytime downwelling longwave radiation. J. Appl. Meteorol. 38, 474–480.

Danielson, J.J., Gesch, D.B., 2011. Global multi-resolution terrain elevation data 2010 (GMTED2010). In: US Geological Survey.

Darnell, W.L., Gupta, S.K., Staylor, W.F., 1983. Downward Longwave radiation at the surface from satellite measurements. J. Clim. Appl. Meteorol. 22, 1956–1960.

Diak, G.R., Bland, W.L., Mecikalski, J.R., Anderson, M.C., 2000. Satellite-based estimates of longwave radiation for agricultural applications. Agric. For. Meteorol. 103, 349–355.

Doutriaux-Boucher, M., Sèze, G., 1998. Significant changes between the ISCCP C and D cloud climatologies. Geophys. Res. Lett. 25, 4193–4196.

Ellingson, R.G., 1995. Surface longwave fluxes from satellite observations: a critical review. Remote Sens. Environ. 51, 89–97.

Emde, C., Buras-Schnell, R., Kylling, A., Mayer, B., Gasteiger, J., Hamann, U., Kylling, J., Richter, B., Pause, C., Dowling, T., Bugliaro, L., 2016. The libRadtran software package for radiative transfer calculations (version 2.0.1). Geosci. Model Dev. 9, 1647–1672.

Forman, B.A., Margulis, S.A., 2009. High-resolution satellite-based cloud-coupled estimates of total downwelling surface radiation for hydrologic modelling applications. Hydrol. Earth Syst. Sci. 13, 969–986.

Forsythe, J.M., Haar, T.H.V., Reinke, D.L., 2000. Cloud-base height estimates using a combination of meteorological satellite imagery and surface reports. J. Appl. Meteorol. 39, 2336–2347.

Fu, Q., Liou, K.N., Cribb, M.C., Charlock, T.P., Grosssman, A., 1997. Multiple scattering parameterization in thermal infrared radiative transfer. J. Atmos. Sci. 54, 2799–2812.

Gelaro, R., McCarty, W., Suárez, M.J., Todling, R., Molod, A., Takacs, L., Randles, C.A., Darmenov, A., Bosilovich, M.G., Reichle, R., Wargan, K., Coy, L., Cullather, R., Draper, C., Akella, S., Buchard, V., Conaty, A., da Silva, A.M., Gu, W., Kim, G.-K., Koster, R., Lucchesi, R., Merkova, D., Nielsen, J.E., Partyka, G., Pawson, S., Putman, W., Rienecker, M., Schubert, S.D., Sienkiewicz, M., Zhao, B., 2017. The modern-era retrospective analysis for research and applications, version 2 (MERRA-2). J. Clim. 30, 5419–5454.

Gui, S., Liang, S., Li, L., 2010. Evaluation of satellite-estimated surface longwave radiation using ground-based observations. J. Geophys. Res. 115.

Guo, Y., Cheng, J., Liang, S., 2019. Comprehensive assessment of parameterization methods for estimating clear-sky surface downward longwave radiation. Theor. Appl. Climatol. 135, 1045–1058.

Gupta, S.K., 1989. A parameterization for longwave surface radiation from sun-synchronous satellite data. J. Clim. 2, 305–320.

Gupta, S.K., Darnell, W.L., Wilber, A.C., 1992. A parameterization for Longwave surface radiation from satellite data: recent improvements. J. Appl. Meteorol. 31, 1361–1367.

Gupta, S.K., Whitlock, C.H., Ritchey, N.A., Wilber, A.C., 1997. Clouds and the Earth's Radiant Energy System (CERES)algorithm theoretical basis document: an algorithm for longwave surface radiation budget for total skies (subsystem 4.6.3). https://ceres.larc.nasa.gov/documents/ATBD/pdf/r2_2/ceres-atbd2.2-s4.6.3.pdf Accessed date: 1 October 2019.

Gupta, S.K., Kratz, D.P., Wilber, A.C., Nguyen, L.C., 2004. Validation of parameterized algorithms used to derive TRMM CERES surface radiative fluxes. J. Atmos. Ocean. Technol. 21, 742–752.

Gupta, S.K., Kratz, D.P., Stackhouse, P.W., Wilber, A.C., Zhang, T., Sothcott, V.E., 2010. Improvement of surface Longwave flux algorithms used in CERES processing. J. Appl. Meteorol. Climatol. 49, 1579–1589.

Holton, J.R., 1973. An introduction to dynamic meteorology. Am. J. Phys. 41, 752–754.

Kiehl, J.T., Trenberth, K.E., 1997. Earth's annual global mean energy budget. Bull. Am. Meteorol. Soc. 78, 197–208.

Kimball, B.A., Idso, S.B., 1982. A model of thermal radiation from partly cloudy and overcast skies. Water Resour. Res. 18, 93–936.

King, M.D., Tsay, S.-C., Platnick, S.E., Wang, M., Liou, K.-N., 1997. Cloud retrieval algorithms for MODIS: optical thickness, effective particle radius, and thermodynamic phase. MODIS Algorithm Theoretical Basis Document 1997.

King, M.D., Platnick, S., Menzel, W.P., Ackerman, S.A., Hubanks, P.A., 2013. Spatial and temporal distribution of clouds observed by MODIS Onboard the Terra and Aqua satellites. IEEE Trans. Geosci. Remote Sens. 51, 3826–3852.

Konzelmann, T., van de Wal, R.S., Greuell, W., Bintanja, R., Henneken, E.A., Abe-Ouchi, A., 1994. Parameterization of global and longwave incoming radiation for the Greenland ice sheet. Glob. Planet. Chang. 9, 143–164.

Kratz, D.P., Gupta, S.K., Wilber, A.C., Sothcott, V.E., 2020. Validation of the CERES edition-4A surface-only flux algorithms. J. Appl. Meteorol. Climatol. 59, 281–295.

Lhomme, J.P., Vacher, J.J., Rocheteau, A., 2007. Estimating downward long-wave radiation on the Andean Altiplano. Agric. For. Meteorol. 145, 139–148.

Liang, S., Wang, K., Zhang, X., Wild, M., 2010. Review of estimation of land surface radiation and energy budgets from ground measurements, remote sensing and model simulation. IEEE J. Selected Topics in Earth Observations and Remote Sensing 3, 225–240.

Mace, G.G., Zhang, Q., Vaughan, M., Marchand, R., Stephens, G., Trepte, C., Winker, D., 2009. A description of hydrometeor layer occurrence statistics derived from the first year of merged Cloudsat and CALIPSO data. J. Geophys. Res. 114.

Mao, F., Pan, Z., Henderson, D.S., Wang, W., Gong, W., 2018. Vertically resolved physical and radiative response of ice clouds to aerosols during the Indian summer monsoon season. Remote Sens. Environ. 216, 171–182.

Maykut, G.A., Church, P.E., 1973. Radiation climate of Barrow Alaska, 1962–66. J. Appl. Meteorol. 12, 620–628.

Menzel, W.P., Frey, R.A., & Baum, B.A. (2015). Cloud top properties and cloud phase algorithm theoretical basis document. https://atmosphere-imager.gsfc.nasa.gov/sites/default/files/ModAtmo/MOD06-ATBD_2015_05_01_2.pdf, Accessed date: 1 August 2019.

Miller, S.D., Forsythe, J.M., Partain, P.T., Haynes, J.M., Bankert, R.L., Sengupta, M., Mitrescu, C., Hawkins, J.D., Vonder Haar, T.H., 2014. Estimating three-dimensional cloud structure via statistically blended satellite observations. J. Appl. Meteorol. Climatol. 53, 437–455.

Miller, S.D., Noh, Y.-J., Forsythe, J.F., Seaman, C.J., Li, Y., Heidinger, A.K., Lindsey, D.T., 2019. Algorithm Theoretical Basis Document: AWG Cloud Base Algorithm. NOAA NESDIS center for satellite applications and research. https://www.star.nesdis.noaa.gov/jpss/documents/ATBD/ATBD_EPS_Cloud_ACHA_v3.0.pdf.

Minnis, P., Heck, P.W., Harrison, E.F., 1990a. The 27–28 October 1986 FIRE IFO cirrus case study: cloud parameter fields derived from satellite data. Mon. Weather Rev. 118, 2426–2447.

Minnis, P., Young, D.F., Sassen, K., Alvarez, J.M., Grund, C.J., 1990b. The 27–28 October 1986 FIRE IFO cirrus case study: cirrus cloud parameter relationships derived from satellite and lidar data. Mon. Weather Rev. 118, 2402–2425.

Minnis, P., Smith Jr., W.L., Garber, D.P., Ayers, J.K., Doelling, D.R., 1995. Cloud Properties Derived from GOES-7 for spring 1994 ARM Intensive Observing Period Using Version 1.0. 0 of ARM Satellite Data Analysis Program. NASA; Hampton, VA United States.

Minnis, P., Sun-Mack, S., Young, D.F., Heck, P.W., Garber, D.P., Chen, Y., Spangenberg, D.A., Arduini, R.F., Trepte, Q.Z., Smith, W.L., Ayers, J.K., Gibson, S.C., Miller, W.F., Hong, G., Chakrapani, V., Takano, Y., Liou, K.-N., Xie, Y., Yang, P., 2011. CERES Edition-2 cloud property retrievals using TRMM VIRS and Terra and Aqua MODIS data—part I: algorithms. IEEE Trans. Geosci. Remote Sens. 49, 4374–4400.

Minns, P., Heck, P.W., Young, D.F., Fairall, C.W., Snider, J.B., 1992. Stratocumulus cloud properties derived from simultaneous satellite and island-based instrumentation during FIRE. J. Appl. Meteorol. 31, 317–339.
Niemelä, S., Räisänen, P., Savijärvi, H., 2001. Comparison of surface radiative flux parameterizations: part I: Longwave radiation. Atmos. Res. 58, 1–18.
Nussbaumer, E.A., Pinker, R.T., 2012. Estimating surface longwave radiative fluxes from satellites utilizing artificial neural networks. J. Geophys. Res.-Atmos. 117 (n/a-n/a).
Platnick, S., King, M.D., Ackerman, S.A., Menzel, W.P., Baum, B.A., Riedi, J.C., Frey, R.A., 2003. The MODIS cloud products: algorithms and examples from terra. IEEE Trans. Geosci. Remote Sens. 41, 459–473.
Prata, A.J., 1996. A new long-wave formula for estimating downward clear-sky radiation at the surface. Q. J. R. Meteorol. Soc. 122, 1127–1151.
Rao, Y., Liang, S., Wang, D., Yu, Y., Song, Z., Zhou, Y., Shen, M., Xu, B., 2019. Estimating daily average surface air temperature using satellite land surface temperature and top-of-atmosphere radiation products over the Tibetan plateau. Remote Sens. Environ. 234, 111462.
Ricchiazzi, P., Yang, S., Gautier, C., Sowle, D., 1998. SBDART: a research and teaching software tool for plane-parallel radiative transfer in the Earth's atmosphere. Bull. Am. Meteorol. Soc. 79, 2101–2114.
Saltelli, A., Tarantola, S., Chan, K., 1999. A quantitative model-independent method for global sensitivity analysis of model output. Technometrics 41, 39–56.
SBDART User guide, 2007. http://irina.eas.gatech.edu/EAS880_Fall2007/User_guide_SBDART_input.pdf Accessed date: 1 August 2018.
Schmetz, P., Schmetz, J., Raschke, E., 1986. Estimation of daytime downward longwave radiation at the surface from satellite and grid point data. Theor. Appl. Climatol. 37, 136–149.
Seemann, S.W., Borbas, E.E., Knuteson, R.O., Stephenson, G.R., Huang, H.-L., 2008. Development of a global infrared land surface emissivity database for application to clear sky sounding retrievals from multispectral satellite radiance measurements. J. Appl. Meteorol. Climatol. 47, 108–123.
Stephens, G.L., Vane, D.G., Boain, R.J., Mace, G.G., Sassen, K., Wang, Z., Illingworth, A.J., O'Connor, E.J., Rossow, W.B., Durden, S.L., Miller, S.D., Austin, R.T., Benedetti, A., Mitrescu, C., 2002. THE CLOUDSAT MISSION AND THE A-TRAIN: a new dimension of space-based observations of clouds and precipitation. Bull. Am. Meteorol. Soc. 83, 1771–1790.
Stephens, G.L., Vane, D.G., Tanelli, S., Im, E., Durden, S., Rokey, M., Reinke, D., Partain, P., Mace, G.G., Austin, R., L'Ecuyer, T., Haynes, J., Lebsock, M., Suzuki, K., Waliser, D., Wu, D., Kay, J., Gettelman, A., Wang, Z., Marchand, R., 2008. CloudSat mission: performance and early science after the first year of operation. J. Geophys. Res. 113.
Stephens, G.L., Wild, M., Stackhouse, P.W., L'Ecuyer, T., Kato, S., Henderson, D.S., 2012. The global character of the flux of downward Longwave radiation. J. Clim. 25, 2329–2340.
Stowe, L.L., Davis, P.A., McClain, E.P., 1999. Scientific basis and initial evaluation of the CLAVR-1 global clear/cloud classification algorithm for the advanced very high resolution radiometer. J. Atmos. Ocean. Technol. 16, 656–681.
Sun, X.J., Li, H.R., Barker, H.W., Zhang, R.W., Zhou, Y.B., Liu, L., 2016. Satellite-based estimation of cloud-base heights using constrained spectral radiance matching. Q. J. R. Meteorol. Soc. 142, 224–232.
Takara, E.F., Ellingson, R.G., 2000. Broken cloud field longwave-scattering effects. J. Atmos. Sci. 57, 1298–1310.
Tang, B., Li, Z.-L., 2008. Estimation of instantaneous net surface longwave radiation from MODIS cloud-free data. Remote Sens. Environ. 112, 3482–3492.
Trenberth, K.E., Fasullo, J.T., Kiehl, J., 2009. Earth's global energy budget. Bull. Am. Meteorol. Soc. 90, 311–323.
Trigo, I.F., Barroso, C., Viterbo, P., Freitas, S.C., Monteiro, I.T., 2010. Estimation of downward long-wave radiation at the surface combining remotely sensed data and NWP data. J. Geophys. Res.-Atmos. 115, D24118.
Viúdez-Mora, A., Costa-Surós, M., Calbó, J., González, J.A., 2015. Modeling atmospheric longwave radiation at the surface during overcast skies: the role of cloud base height. J. Geophys. Res.-Atmos. 120, 199–214.
Wang, J., Rossow, W.B., Zhang, Y., 2000. Cloud vertical structure and its variations from a 20-Yr global Rawinsonde dataset. J. Clim. 13, 3041–3056.
Wang, K., Dickinson, R.E., 2013. Global atmospheric downward longwave radiation at the surface from ground-based observations, satellite retrievals, and reanalyses. Rev. Geophys. 51, 150–185.
Wang, T., Shi, J., Yu, Y., Husi, L., Gao, B., Zhou, W., Ji, D., Zhao, T., Xiong, C., Chen, L., 2018. Cloudy-sky land surface longwave downward radiation (LWDR) estimation by integrating MODIS and AIRS/AMSU measurements. Remote Sens. Environ. 205, 100–111.
Wang, W., Liang, S., 2009. Estimation of high-spatial resolution clear-sky longwave downward and net radiation over land surfaces from MODIS data. Remote Sens. Environ. 113, 745–754.
Wang, Z. (2019). CloudSat 2B-CLDCLASS-LIDAR product process description and interface control document. http://www.cloudsat.cira.colostate.edu/sites/default/files/products/files/2B-CLDCLASS-LIDAR_PDICD.P1_R05.rev0_.pdf, Accessed date: 1 May 2020.
Wang, Z., & Sassen, K. (2007). Level 2 cloud scenario classification product process description and interface control document. http://www.cloudsat.cira.colostate.edu/sites/default/files/products/files/2C-ICE_PDICD.P1_R05.rev0_.pdf, Accessed date: 1 May 2020.
Wielicki, B.A., Barkstrom, B.R., Baum, B.A., Charlock, T.P., Green, R.N., Kratz, D.P., Lee, R.B., et al., 1998. Clouds and the earth's radiant energy syetem (CERES): algorithm overview. In: IEEE Transactions on Geoscience and Remote Sensing. *36*. pp. 1127–1141.
Wild, M., Ohmura, A., Gilgen, H., Morcrette, J.J., Slingo, A., 2001. Evaluation of downward longwave radiation in general circulation model. J. Clim. 14, 3227–3239.
Willett, H.C., 1933. American Air Mass Properties. Massachusetts Institute of Technology and Woods Hole Oceanographic Institution.
Yu, S., Xin, X., Liu, Q., Zhang, H., Li, L., 2018. Comparison of cloudy-sky downward longwave radiation algorithms using synthetic data, ground-based data, and satellite data. J. Geophys. Res.-Atmos. 123, 5397–5415.
Zhang, T., Stackhouse, P.W., Gupta, S.K., Cox, S.J., Mikovitz, J.C., 2015. The validation of the GEWEX SRB surface longwave flux data products using BSRN measurements. J. Quant. Spectrosc. Radiat. Transf. 150, 134–147.
Zhang, Y., Rossow, W.B., Lacis, A.A., Oinas, V., Mishchenko, M.I., 2004. Calculation of radiative fluxes from the surface to top of atmosphere based on ISCCP and other global data sets: refinements of the radiative transfer model and the input data. J. Geophys. Res. 109.
Zhang, Y.C., Rossow, W.B., Lacis, A.A., 1995. Calculation of surface and top of atmosphere radiative fluxes from physical quantities based on ISCCP data sets: 1. Method and sensitivity to input data uncertainties. J. Geophys. Res. - Atmos. 100, 1149–1165.
Zhou, D.K., Larar, A.M., Liu, X., Smith, W.L., Strow, L.L., Yang, P., Schlussel, P., Calbet, X., 2011. Global land surface emissivity retrieved from satellite Ultraspectral IR measurements. IEEE Trans. Geosci. Remote Sens. 49, 1277–1290.
Zhou, Y., Cess, R.D., 2001. Algorithm development strategies for retrieving the downwelling longwave flux at the Earth's surface. J. Geophys. Res.-Atmos. 106, 12477–12488.
Zhou, Y., Kratz, D.P., Wilber, A.C., Gupta, S.K., Cess, R.D., 2007. An improved algorithm for retrieving surface downwelling longwave radiation from satellite measurements. J. Geophys. Res. 112, D15102.
Zhu, M., Yao, T., Yang, W., Xu, B., Wang, X., 2017. Evaluation of parameterizations of incoming Longwave radiation in the High-Mountain region of the Tibetan plateau. J. Appl. Meteorol. Climatol. 56, 833–848.